Investigation of Ground Effect on the Wingtip Vortices Generated Behind a Swept and Tapered Wing

Samson Paul Pinto

Supervisor: Prof. Tim Lee

Department of Mechanical Engineering

McGill University

Montreal, Quebec

July 2021

A thesis submitted to McGill University in partial fulfillment of the requirements of the degree of Master of Science.

Abstract

An experimental study of the effect of ground proximity on wingtip vortices has been conducted for swept and tapered wing with NACA 0015 profile over a stationary flat surface in a subsonic wind tunnel. The spatial growth and development of the vortex system generated by the swept and tapered wing with and without winglet arrangement have also been studied. It has been noted that with the reduction in ground proximity, the vortex system moved outward along the spanwise direction by 20% of the wingspan, and it moved closer to the ground. In close ground proximity, vortex rebound occurred due to a lack of space for movement of the vortex. For ground proximity of 15% root chord, a co-rotating ground vortex has been observed, and at 5% of root chord, a counter-rotating secondary vortex has been noticed. The interaction of these different vortices has led to the change of the shape of the entire vortex system.

The calculation of lift-induced drag has also been computed using vw-crossflow measurements in the near wake region. It has been observed that the lift-induced drag decreases with reducing ground distance. At ground proximity of 5% root chord distance, a 20% decrease in lift-induced drag is seen compared to lift-induced drag outside ground effect. Also, with the addition of a 90° winglet, an average decrease of 5% lift-induced drag is seen when compared to the wing without a winglet.

The lift coefficient has been estimated using the circulation of the vortex system both inside and outside ground effect. It has been noted that there is a 53% increase in the coefficient of lift at 5% ground proximity compared to the coefficient of lift outside ground effect. It has been found that the trend of coefficient of lift versus the ground distance matches the trend of other wing planforms

and increases exponentially as the ground proximity decreases below 10% root chord. It has been concluded that the swept wing with a 90° winglet arrangement has been found to outperform all other arrangements.

Résumé

Une étude expérimentale de l'effet de la proximité du sol sur les tourbillons d'extrémité d'aile a été menée pour une aile en flèche et conique avec un profil NACA 0015 sur une surface plane stationnaire dans une soufflerie subsonique. La croissance spatiale et le développement du système de vortex généré par l'aile en flèche et effilée avec et sans disposition d'ailettes ont également été étudiés. Il a été noté qu'avec la réduction de la proximité du sol, le système de vortex s'est déplacé vers l'extérieur dans le sens de l'envergure de 20 % de l'envergure, et il s'est rapproché du sol. À proximité du sol, le rebond du vortex s'est produit en raison d'un manque d'espace pour le mouvement du vortex. Pour une proximité du sol de 15 % de la corde de racine, un vortex au sol co-rotatif a été observé, et à 5 % de la corde de racine, un vortex secondaire contrarotatif a été remarqué. L'interaction de ces différents vortex a conduit à la modification de la forme de l'ensemble du système vortex.

Le calcul de la traînée induite par la portance a également été calculé à l'aide de mesures d'écoulement transversal vw dans la région de sillage proche. Il a été observé que la traînée induite par la portance diminue avec la réduction de la distance au sol. À proximité du sol de 5% de la distance de la corde de racine, une diminution de 20% de la traînée induite par la portance est observée par rapport à la traînée induite par la portance en dehors de l'effet de sol. De plus, avec l'ajout d'un winglet à 90°, une diminution moyenne de 5% de la traînée induite par la portance est observée par rapport à l'aile sans winglets.

Le coefficient de portance a été estimé en utilisant la circulation du système tourbillonnaire à la fois à l'intérieur et à l'extérieur de l'effet de sol. Il a été noté qu'il y a une augmentation de 53 % du coefficient de portance à 5 % de la proximité du sol par rapport au coefficient de portance hors

effet de sol. Il a été constaté que la tendance du coefficient de portance par rapport à la distance au sol correspond à la tendance d'autres formes de plan d'aile et augmente de façon exponentielle lorsque la proximité du sol diminue en dessous de 10 % de la corde d'emplanture. Il a été conclu que l'aile en flèche avec un agencement d'ailettes à 90° s'est avérée surpasser tous les autres agencements.

Acknowledgments

A successful thesis is always in the mind of the professor and the hands of the student. I consider myself lucky to have been supervised by **Prof. Tim Lee**, and under his guidance, I felt like my mind was being shaped with a chisel called Aerodynamics. I want to thank him for his constructive supervision and valuable insights throughout the project. His patience, motivation and strong knowledge of the subject have helped me through this journey at McGill University.

I want to thank my twin **Salmon Ben Pinto** for not thinking twice about investing his hard-earned money to support me to study in Canada. I also extend my gratitude to my brother **Nived Joseph** for his continued belief in me even when I did not believe in myself. I want to thank my mother and my father for their continued support throughout my education and for not setting any boundaries around me when it comes to education.

Finally, I would like to thank **Anan Lu**, my predecessor and my guide, for this project. She taught me the basics I needed to know, and in the crucial moments of the pandemic, she never hesitated to take the time to show me the right way.

The experimental credits of this work belong to **Anan Lu** and **Josef Qui.**

To my twin,

Salmon Ben Pinto

For being the foundation of our family, for backing up every position, and for being the perfect

son to our parents.

Table of Contents

List of Figures

List of Tables

List of Symbols

C_L	Coefficient of lift		S	Area of the wing
C_D	Coefficient of Drag		AR	Aspect ratio (b^2/S)
C_l	Sectional lift coefficient of the airfoil		AR_{eff}	Effective aspect ratio
C_d	Sectional drag coefficient of the airfoil		α	Angle of attack
$C_{L,IGE}$	Lift coefficient inside ground effect (C_{L1}, C_{L2} and C_{L3})		λ	Taper ratio (c_r/c_t)
$C_{L,OGE}$	Lift coefficient outside ground effect		$\Lambda_{c/4}$	Sweep angle at ¼ chord
C_{Di}	Coefficient of lift-induced drag		x	Streamwise distance
D_i	Lift-induced drag		y	Longitudinal distance
Re	Chord Reynold number		z	Spanwise distance
c_r	Root chord of the swept wing		ζ_{peak}	Peak vorticity
c_t	Tip chord of the swept wing		ζ	Streamwise vorticity
c_{wr}	Root chord of the winglet		u	Axial velocity
c_{wt}	Tip chord of the winglet		U	Free stream velocity
b	Span of the wing		u/U	Non-dimensional axial velocity
b'	Effective span		v_θ	Tangential velocity
$b_{c/4}$	Span at ¼ chord		Γ_o	Total circulation of the vortex
h	Distance between the trailing edge of the wing and the surface boundary		Γ_c	Circulation of the vortex core
h/c_r	Ground distance ratio			

Abbreviation

OGE	Outside ground effect	TV	Trailing vortex
IGE	Inside ground effect	JV	Junction vortex
GEV	Ground effect vehicle	SV	Secondary vortex
WIG	Wing in ground effect	GV	Ground vortex
GE	Ground effect		

1. Introduction

A wingtip vortex is formed when a wing cruises through a freestream, and air from the high-pressure lower surface of the wing is sucked into the low-pressure upper surface over the tip of the wing. This air movement due to elevated pressure difference between the two surfaces initiates a three-dimensional rollup that grows in strength, shape and size and propagates in the form of a swirl. As the swirl reaches the trailing edge of the wing, a vortex is generated, and it detaches from the wing and propagates downstream of the wing. This so-called wing tip vortex will circulate for hundreds of chord lengths before becoming weaker and eventually perishing. Due to its rotating nature, it will cause problems to flight safety and cause a considerable drag due to the enormous energy spent in the formation of the shape of the vortex. Figure 1-1 shows how the vortex forms and evolves into space downstream of the wing. If another flying object or species comes in the range of the downwash of this wingtip, it will experience a severe imbalance and rugged maneuverability, and hence this wingtip vortex needs to be addressed.

Wingtip vortices are produced in aircraft and other airborne vehicles regardless of the height of their flight. However, when these airborne vehicles fly close to a surface boundary, a different phenomenon emerges. Due to the presence of the surface boundary, the air below the wing experiences a reaction from the surface boundary. This air reaction generates a floating effect called a "dynamic air cushion," and the vehicle is now said to be in ground effect (GE). Specific vehicles are designed to take advantage of this GE and fabricated to fly close to the surface boundary, maybe water or earth. These vehicles are called ground effect vehicles (GEVs) or wing-in-ground effect (WIG) craft. The closer these vehicles fly to the ground, the higher is the GE felt by these vehicles, and the better is the ability to float on the surface boundary (Yun et al. (2010)).
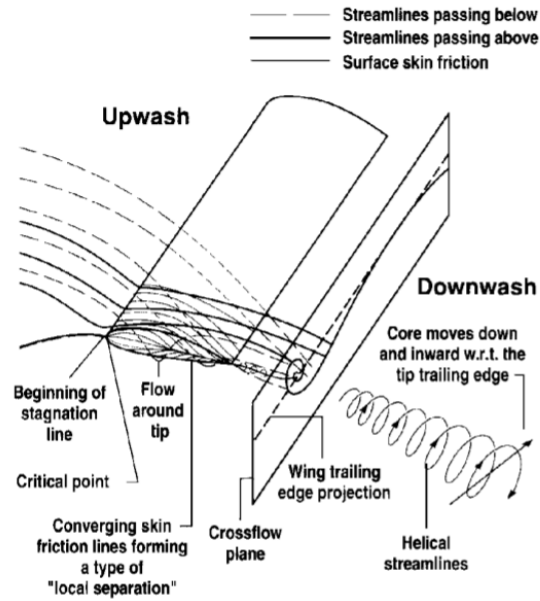
Figure 1-1 Schematic depicting the formation of the wingtip vortex (Chow et al. (1997))

The pressure distribution profiles on airborne vehicles' wings are based on whether a specific vehicle is flying outside ground effect (OGE) or inside ground effect (IGE). Figure 1-2 shows the distribution of pressure on the surface of the wing's airfoil section. When the vehicle's wing is in the IGE case, there is a restricted flow path for the air to move below the wing. Due to this, the dynamic pressure of the air below the wing is converted into static pressure. This rise in static pressure is called "ram pressure," which promotes the generation of lift in ground effect. In GE,
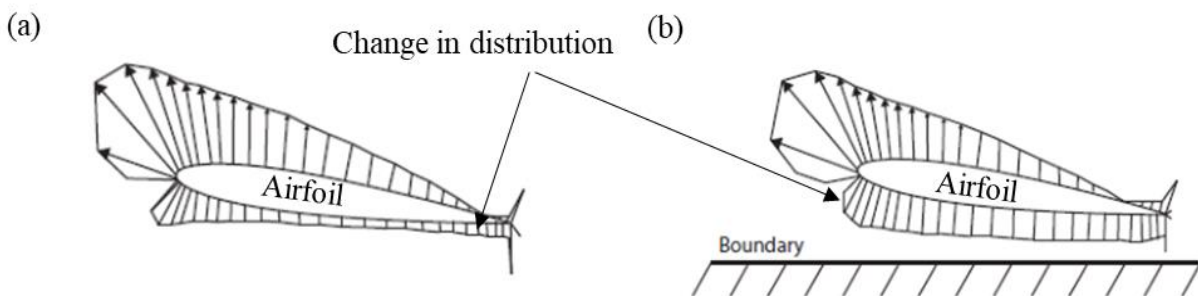
Figure 1-2 Pressure distribution over the surface of the airfoil, (a) in OGE case, and (b) in IGE case (Ko (2017))

the change in pressure distribution that creates an increase in the lift also creates other changes in the wing's aerodynamic flow properties. Due to the presence of the ground, the surge in static pressure reduces the downwash, which directly results in the reduction of the lift-induced drag. Due to this reduction, there is a betterment in the lift-to-drag ratio of the WIG craft (Ko (2017)).

The presence of the ground effect also affects the wingtip vortices. It is a very well-known fact that a downwash is created due to the wingtip vortices. The magnitude of the downwash velocity is relatively high when it is at the tip of the wing and reduced as the downwash advances far downstream. This downwash is responsible for the change in lift-induced drag, which is a function of the downwash angle. Due to the presence of the surface boundary, the downwash produced by the wingtip vortices is lower since there is no gap for them to evolve into a bigger size. Hence the downwash angle is also lower, and this reduces the lift-induced drag. The excessive energy that would be spent as a result of the formation of more prominent vortices in the OGE case is now restored, and only a part of it is spent in pushing the wingtip vortices outwards in the spanwise direction. As a result, the effective aspect ratio of the wing rises, giving rise to increased lift. This change in the shape of wingtip vortices due to GE is shown in Figure 1-3 (Yun et al. (2010)).
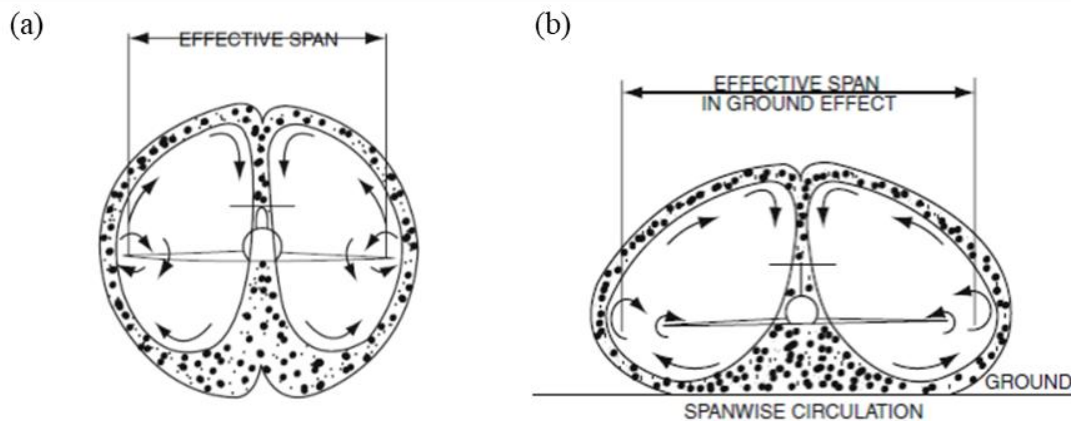
Figure 1-3 Conceptual sketches of wingtip vortices, (a) in OGE case, and (b) in IGE case (Yun et al. (2010))

3

Another critical change in property that causes problems in the maneuverability of a WIG craft is the shift of the aerodynamic center of the wing due to the presence of the ground effect. There is a minimal shift in the aerodynamic center of a given wing in the OGE case for wings with symmetric airfoils. There is a net change in the aerodynamic center for wings with cambered airfoils, but the change does not vary continuously in the OGE case. However, in the IGE case, there is a significant shift in the aerodynamic center of the wing due to the pressure variations created under the wing regardless of the change in the airfoil shape of the wing. Hence the WIG crafts often require specific attachments to improve the control of the craft. The WIG crafts have been designed in the past based on square or rectangular wing platforms, and reverse delta wing platforms with various attachments have been further discussed in the section below.

Much research on square or rectangular wings in GE is already done, and the data available on its performance in GE is quite large. However, almost all aircraft today use swept wings; their performance in ground effect relatively remains an unestablished topic of research. It is also worth mentioning that the delta wing and the reverse delta wing in ground effect have also been studied to an extent more remarkable than the swept wing. Hence the main topic of this study will remain restricted to the swept wing in ground effect. To the best of the author's knowledge and reach, almost no literature is available to study the ground effect on the swept wing. Hence, to gauge the swept wing's performance, the literature available on other wing planforms in ground effect has also been studied.

As mentioned above, the intensity of the wingtip vortices is directly proportional to the change in downwash angle. If the magnitude of these tip vortices can somehow be decreased, then there is a direct decrease in lift-induced drag due to a decrease in downwash angle, which appreciates the wing's aerodynamic performance. It is well known that commercial aircraft have winglets attached

4

to the end of the wing; these winglets split the trailing vortex (TV), thereby dividing the trailing vortex into smaller vortices of lesser magnitude. Hence there is a restoration of some energy that would have been otherwise lost due to the formation of more prominent vortices, and hence there is a net decrease in lift-induced drag. There is much research available in the literature for the performance of the wings with winglets in OGE. However, almost no data is available when it comes to their performance in ground effect. Hence, this study also concentrates on the effect of ground proximity on the swept wing's performance with winglets. Before directly diving into the literature review, a discussion on the development of two concepts becomes necessary. The first one is the development of two main types of WIG craft, which is discussed in the following section. The second one is the distinction of two dominant types of ground effects, briefly introduced in section 1.2 and further elaborated in Chapter 2.

1.1. Wing-in-ground effect (WIG) craft

Even though many WIG crafts have been built in the past, two main types of WIG craft stand out based on their operation concept. The first one is the square or rectangular wing type GEV with a large tail stabilizer (i.e., Russian Ekranoplan), and the second one is the reverse delta wing type GEV with an anhedral (i.e., Lippisch-type). Rostislav Alexeyev designed one of the most famous Russian Erkranoplan known as the "KM" (Korabl Maket), and it was tested in 1967. The KM was

Figure 1-4 Photographs of (a) KM, (b) RFB X-114 (Yun et al. (2010)), and (c) WSH 500 (Brochure Wingship 500 (2014))

a 544-tons vehicle that had a wingspan of 37.6 m. The vehicle's total length was 92 m, and its height was 21.4 m and is shown in Figure 1-4. It floated about the surface at the height of 5 to 10 m, and it cruised at a speed of 500 km/h. The significant nose-down pitching moment due to shift in the aerodynamic center of the Ekranoplan was overcome by huge tailplanes that were half the main wing area. Even though it was a successful GEV, there were specific efficiency degrading factors due to its design (Ko. (2017)).

Alexander Lippisch built the first reverse delta wing GEV with an anhedral; it was called the X-113 and was built in 1973 in Germany by RBF. The X-113 had a fuselage with stepped planing lower surfaces, and the main wing of the craft was designed to create a dynamic air cushion. The roll of the GEV was maintained by providing winglets with 60° dihedral angles, which were mounted on the floats attached to the ends of the main wing. A two-cylinder Nelson engine with 38 kW of brake power was used to drive a twin-blade propeller. It was successfully tested and had a cruising speed of 124 km/h. Based on the success of the X-113, another six-seater model known as the RFB X-114 was built in 1976, which is shown in Figure 1-4. The RFB X-114 had a wing reverse delta wing with 19° anhedral and could cruise at a speed of 144 km/h (Yun et al. (2010)). This RFB X-114 was termed a successful GEV, and based on RFB X-114, Wing ship technology corporation built WSH-500, and its first prototype was tested in 2011 in South Korea. Figure 1-4 shows the WSH-500, a 50-seater GEV with a body of length 28.5 m. The wingspan of the GEV is 27 m; it has a take-off weight of 17.1 tons and can cruise at a speed of 180 km/h at an altitude of 1 to 5 m (Ko. (2017)).

1.2. Types of ground effect

There are two dominant types of ground effect: chord-dominated ground effect and span-dominated ground effect. Chord-dominated ground effect is for airfoils with no free end effects.

6

At a positive angle of attack for 2-D airfoils, proximity to surface boundary generally causes a high-pressure distribution on the airfoil's lower surface, leading to an increasing lift, nose-down pitching moment, and lift-to-drag ratio; this phenomenon is called the chord-dominated ground effect. Span-dominated ground effect is for finite wings with free end effects. At a positive angle of attack for 3-D finite wings, proximity to the ground surface generally leads to an outward push of wingtip vortices, causing a depreciation in the downwash angle and a reduced lift-induced drag; this phenomenon is called the span-dominated ground effect (Qu and Agarwal (2017)). When it comes to understanding ground effect, it is imperative to understand the differences between the ground effect types clearly. Hence these two types of ground effects have been further discussed in the literature.

2. Literature Review

The literature review starts with the emphasis being placed on chord-dominated ground effect and span-dominated ground effect with the aim of understanding the clear difference between them. In section 2.1, cambered and symmetric airfoils are studied to understand how unique they may be in their performance in ground effect. In section 2.2, the ground effect on finite wings, delta wings and reverse delta wings and various attachments added to wingtips to reduce the strength of wingtip vortices are studied. Section 2.3 is a summary based on the observations from the literature. Finally, the objectives of the research are stated in section 2.4.

2.1. Chord-dominated ground effect

Chord-dominated ground effect on the aerodynamic performance of the airfoil is based on parameters such as airfoil profile, angle of attack, type of ground surface, Reynolds number (Re), and type of ground boundary conditions. Different researchers have evaluated the change in aerodynamic properties by chord-dominated ground effect due to change in these parameters. However, for this literature, the parameters are restricted to the airfoil profile (i.e., symmetric and cambered airfoils) and the boundary condition (i.e., stationary ground and moving ground).

Carter (1961) performed an investigation to determine how 11% chord thickness and 22% chord thickness cambered airfoils behaved in ground effect. The experimentation was made with the models of airfoil moving over the water in a towing tank. In order to reduce the effects of the wind tunnel walls and the effects of the boundary layer on the ground at shallow ground distances, a towing tank was used for experimentation instead of the wind tunnel. The results indicated a high value in lift-curve slope and a depreciation in the lift-induced drag, raising the lift-to-drag ratio. It was also noted that the profile drag remained the same with the variety of different airfoils with

8

varying ground distances. With positive values for α, the airfoils had longitudinal stability, and as the height above the ground increased, the stability also increased. Turner (1966) saw a considerable rise in the sectional coefficient of lift C_l with the increase in closeness to the ground in a wind tunnel. The increase in C_l was observed to be 33% at a ground distance of 33% of the non-dimensional height to span ratio. Suh and Ostowari (1988) derived a theoretical formula for C_d and compared it with experimentation in the literature and existing formulas. The derived formula for C_d was in agreement with experimental data for an Oswald efficiency factor of 0.85 ~ 0.9 at an aspect ratio AR = 1 to 4 only. It was noted from the formula that there was a reduction in sectional drag and an increase in the lift to drag ratio in ground proximity for the wings with characteristics as mentioned above. Another major factor noted was the variation in the value of vorticity of the wing that indicated an increased flow separation. Steinbach and Jacob (1991) performed a theoretical investigation with moving ground. The introduction of this moving ground (i.e., slip boundary condition) helped remove the boundary layer developed by a fixed ground, due to which there was a higher flow path and a lower ram pressure. The observations concluded a large flow separation, a significant lift increase, and a significant drag increase at extreme ground proximity.

Hsiun and Chen (1996) numerically studied a NACA 4412 airfoil flow field with a no-slip boundary (i.e., fixed ground) condition at a chord Reynolds number of Re = 3.2×10^5 at an angle of attack α = 15°. It was observed that the flow separation in the IGE case was much greater than the flow separation in OGE. When viscous effects were considered, it was also observed that at higher values of α and extreme ground proximity, a robust circular flow was generated between the leading edge of the airfoil and the ground's surface. Furthermore, when the value of Re was

increased further beyond the value mentioned above, the C_l value increased further for varying ground proximity values.

Moore et al. (2002) measured the C_l and C_d of a rectangular NACA 0012 wing in a rolling road (i. e., moving ground) wind tunnel at Re = 8×10^5. The wing had an AR = 3.01, and the α value was varied from -3° to 15°. Both C_l and C_d were found to increase with decreasing ground distance. However, no significant change in C_d was seen when the rolling road was turned off. The investigators also studied the flow field and noted that at α = 3°, the value of lift coefficient inside ground effect decreased as the wing approached the ground. This reduction was due to the suction effect developed at the lower section of the wing, which resulted from the venturi effect between the lower surface of the wing and the ground. The flow regimes observed in IGE were divided into two, namely, normal ground effect flow regime and ram ground effect flow regime. The flow regime that occurred below h/c < 10% was the ram ground effect flow regime, which had an almost sealed envelope of air between the lower surface of the wing and the ground. The flow regime that occurred above h/c > 10% was the normal ground effect flow regime.

Barber et al. (2002) studied the ground effect of fixed ground and moving ground on the NACA 4412 airfoil numerically and experimentally. This study was based on three central ambiguities noted in their previous study: the correct use of ground boundary conditions, rigid ground boundary conditions for water surfaces, and the right decision between using a potential flow model or considering viscous effects. The following three main conclusions were made. The first was that for numerical simulations, the slip boundary condition is the most suitable one. The second was that for non-rigid surfaces, the surface deformation is not actually due to pressure but due to wingtip vortices. The third one was that the study of ground effect aerodynamics was such that potential flow models do not apply. The simulation results from this study showed that at

extreme surface proximity, the C_l of NACA 4412 airfoil was reducing for a fixed ground boundary but was increasing for a moving ground boundary.

Ahmed and Sharma (2005) experimentally studied the flow characteristics and the aerodynamics of a NACA 0015 airfoil with a chord of 15 cm and a stationary ground setup at a Re = 2.4×10^5. The value of α was varied from 0° to 10° with a changing ground clearance h, normalized by the airfoil chord c, from 5% to 100%. The pressure on the surface of the airfoil was monitored by seven surface pressure taps provided on the surface. It was observed that the lift coefficient was found to increase with the decrease in ground proximity due to the presence of high pressure, as shown in Figure 2-1. However, at small α, the reduction in ground clearance had a decremental
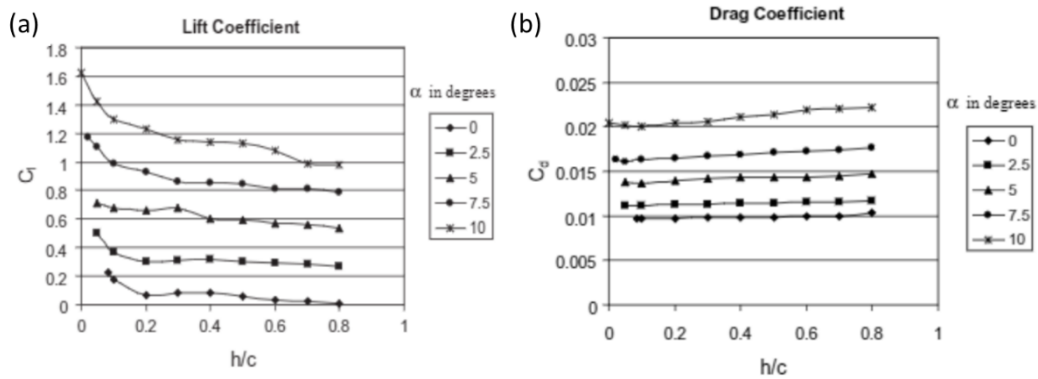
Figure 2-1 (a) Lift coefficient and (b) drag coefficient for varying angle of attacks and ground clearances (Ahmed and Sharma (2005))

effect on the value of the lift coefficient of inside ground effect due to the observed venturi effect. In addition, a loss of upper surface suction was recorded as the airfoil approached the ground. It was concluded that at all α, the pressure drag at proximity to the ground was higher since the high pressure originated from the airfoil's lower surface. Ahmed et al. (2007) experimented with NACA 4412 airfoil with variations in the ground distance between 5% to 100% of the chord and the α value between 0° to 10° at a Re = 3×10^5. At ground proximity of 5% chord and below and α =

0°, a strong suction was observed due to the convergent-divergent passage, which led to a decreased lift. At the same ground distance, a surge in pressure distribution was seen for $\alpha > 4°$, due to which there was an increase in lift force. For $\alpha > 8°$, the increase in the lift was way more significant with decreasing ground proximity. For all values of α, an increase in total drag was seen with decreasing ground proximity.

Luo and Chen (2012) used load cell and surface pressure measurements to investigate the ground effect on the performance of NACA 0015 airfoil in a wind tunnel at a Re = 187,200. The ground was replicated by a perplex plate vertically mounted with a streamwise length and height of 60 cm and 45.7 cm, respectively, which was also the height of the wind tunnel test section. A reduction in lift coefficient was noted for an α of 0° to 6° when the ground distance ratio decreased from 30% to 15%, caused by the channel's venturi effect. The variation of the C_l versus ground distance ratio is shown in Figure 2-2. The slope of the lift curve showed its dependence on the ground distance ratio. In this case, the ground distance between the airfoil and the flat plate was defined at the mid chord of the airfoil instead of the trailing edge, and hence, any changes in α did not affect the distance h. It was concluded that the lift force calculated in the experiment matched the
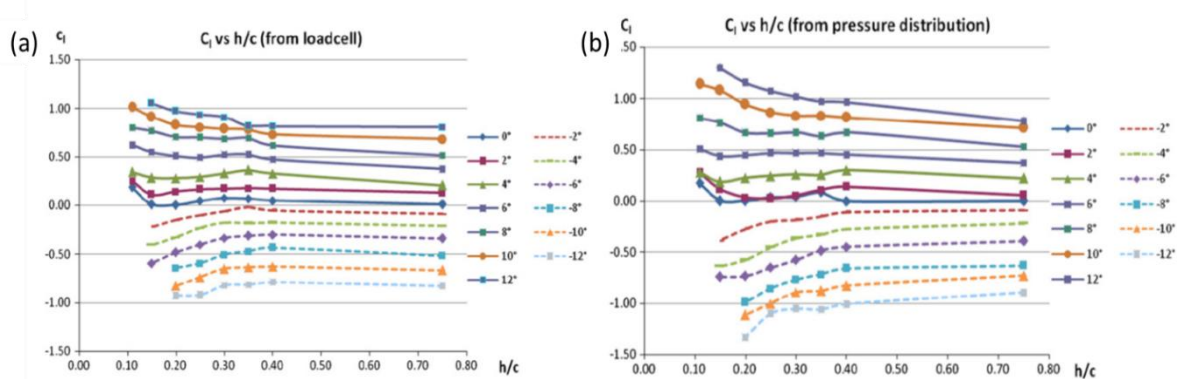
Figure 2-2 Lift coefficient versus ground distance ratio at varying α (a) from load cell, and (b) from pressure distribution (Luo and Chen (2012))

12

magnitude estimated by the thin airfoil theory. Lee and Lee (2014) used a finite-volume-based method to simulate a rectangular wing with NACA 0015 profile and an AR = 6.6, at a chord Re = 1.5×10^6. The results showed an increase in C_l for $\alpha > 4°$; this is because of the ground effect. At $\alpha < 4°$, it was seen that there was a decrease in lift due to the presence of the venturi effect. It was also noted that the critical angle of attack played a vital role in getting the desired lift for a vehicle operating in ground effect.

Lee et al. (2018) experimented with static oscillating NACA 0012 airfoil in ground effect at Re = 9.81×10^4. For values of $\alpha < 6°$, a nose-up pitching moment and depreciation in C_l were seen with static airfoil in ground proximity. Meanwhile, for values of $\alpha > 6°$, a nose-down pitching moment always increases C_l value in ground proximity. Tremblay-Dionne and Lee (2021) studied the discrepancy in the aerodynamic coefficient due to fixed surface and moving surface boundary for a NACA 0012 airfoil by using particle image velocimetry (PIV) and surface pressure measurement at a Re = 9.2×10^4 for a ground distance ratio of 5%, 10% and 20% of chord. For higher angles of α with decreasing ground proximity, the value of C_l was more for moving boundary than fixed ground boundary because of the existence of ground vortex (GV), which originated because of the rolling up of longitudinal boundary layer that accelerated the flow.

Based on the detailed literature review in the above section, a few conclusions were drawn. For symmetric airfoil, the value of C_l was negative for a small value of α at a small ground distance ratio due to the converging-diverging effect (i.e., venturi effect). The negative C_l appeared for both moving and fixed surface boundary conditions. On the contrary, for higher values of α, the sectional lift coefficient C_l was found to increase with decreasing ground proximity for the moving ground boundary condition due to reduced flow blockage and improved pressure distribution underneath the airfoil compared to its fixed ground counterpart. The value of C_d was found to

increase exponentially as the ground approached for both types of surface boundary conditions. Finally, an increased flow separation was observed as the ground approached.

2.2. Span-dominated ground effect

Span-dominated ground effect occurs in 3-D finite wings. The main difference between the 2-D airfoils from the finite wing is that the finite wing has tips over which the flow from the bottom of the wing travels to the top of the wing to balance the pressure difference created during its flight. When this air movement occurs over the tip, a swirling vortex generates from the end of the tip and moves downstream of the wing. Finite rectangular wings and swept-back tapered wings in ground effect are examples of span-dominated ground effect. Meanwhile, the span-dominated ground effect also significantly impacts delta wings and reverse or inverted delta wings. A brief review of the span-dominated ground effect on finite wings is given in the following subsection 2.2.1, followed by subsection 2.2.2 on delta wings and reverse delta wings. Finally, the control of wingtip vortices is given in the last subsection 2.2.3.

2.2.1. Ground effect on finite wings

The ground effect on rectangular wings has been extensively researched, and broad literature is available on them. Harvey and Perry (1971) investigated the semi-rectangular wing in ground effect to understand the descending vortex flow structure. The experiment was done in a moving ground wind tunnel at $Re = 3.47 \times 10^5$. They observed a secondary vortex (SV) forming due to the rolling up of the spanwise boundary layer developed due to the trailing vortex (TV) interaction with the ground. Figure 2-3 shows the conceptual sketch drawn by them, which shows a secondary vortex formation. Ramaprian and Zheng (1997) experimented with NACA 0015 rectangular wing
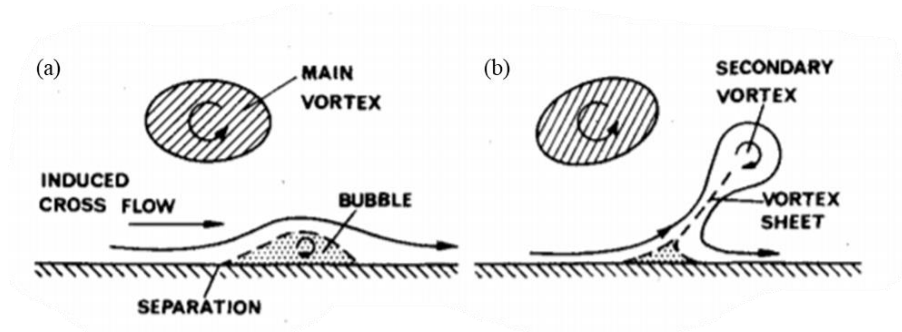
Figure 2-3 (a) Initial separation bubble and (b) formation of secondary vortex (Harvey and Perry (1971))

and used laser doppler velocimetry to study the flow structure in the rollup region. It was noted that the vortex core had a maximum axial velocity at the center, and it decayed to a magnitude close to zero due to turbulent diffusion in the outer part of the vortex at various angles of attack. Except for the outermost part, a significant part of the vortex became nearly axisymmetric beyond a downstream distance of two times chord. Chow et al. (1997) studied the rollup of wing tip vortex of a NACA 0015 rectangular semi-wing at Re $= 4.6 \times 10^6$. It was seen that since there was a favourable pressure gradient due to the development in crossflow velocities in the chordwise distance, there was an acceleration in the vortex core about 1.7 times the free stream. Yeung and Lee (1999) conducted a PIV study with a NACA 0015 wing with adjustable angles of attack. It was found that at an angle of attack of 14°, the wing-tip vortices were highly unsteady, which was in the post-stall region.

Yang et al. (2010) conducted a numerical study with 3-D wings in ground effect. The rectangular wing, delta wing, and forward-swept reverse delta wing were used, as shown in Figure 2-4. It was observed that forward swept reverse delta wing outperformed other wing planforms as it suffers less from wingtip vortices, had a lower drag coefficient and high lift-to-drag ratio, and decreased lift-induced drag. The wing shape prevented the high pressure from exiting through the wingtip; instead, it existed through the trailing edge and contributed to further augmenting the lift. At a
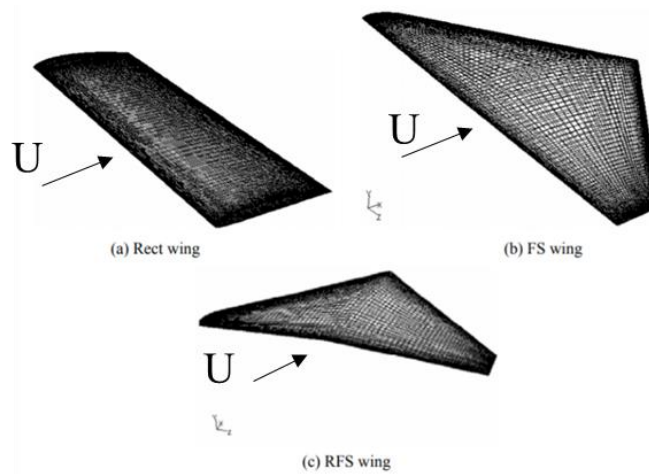
Figure 2-4 3-D computational grids (a) rectangular wing, (b) forward swept delta wing, and (c) forward swept reverse delta wing (Yang et al. (2010)).

ground distance ratio of 5% chord, a nose-down pitching moment was observed for the rectangular wing. A similar study was carried out by Jia et al. (2016). They studied the aerodynamic performance of the banked wing in ground effect using numerical simulation done by FLUENT software. A realizable $k - \varepsilon$ turbulence model was used for simulation at $Re = 3.4 \times 10^6$. An inverted delta wing, a rectangular wing, and a rectangular wing with endplates were used to study the wing's banking in ground effect, as shown in Figure 2-5. The main conclusion of this study was that when a wing is banked, the descending side of the wing produced more lift than the rising
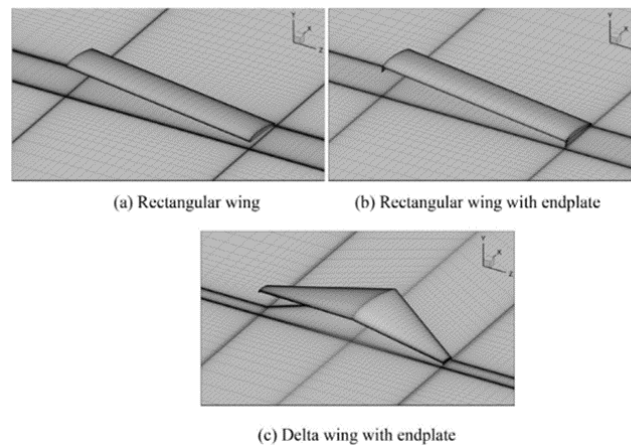
Figure 2-5 3-D wing models in ground effect (Jia et al. (2016))

16

side. The three wings were compared in the same banked position, and it was noted that the rectangular wing required more control as it produced a higher righting moment and adverse yaw moment than other wings.

Lu et al. (2019) experimented with a rectangular wing with a NACA 0015 profile in ground effect. The free stream velocity of U = 15 m/s was used for experimentation, and force balance experiments were conducted with chord c = 28 cm and semi-span of b/2 = 50.8 cm for the wing. The experiment results showed (Figure 2-6) a considerable increase of $C_{L,IGE}$ for a ground distance below 0.6 times chord, at various values of attack α. Lu and Lee (2021) studied the effect of stationary and moving ground boundary conditions on the near wake region of NACA 0012 rectangular semi-wing at Re = 9.2×10^4. The study was carried out at a varying ground distance
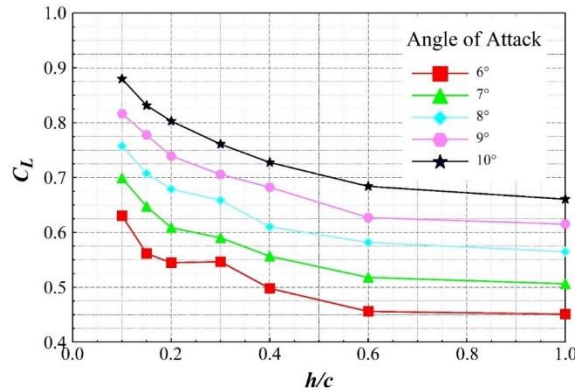
Figure 2-6 Coefficient of lift (C_L) with varying ground distance for a rectangular wing (Lu et al. (2019))

ratio between 60% to 5% chord at a downstream distance ratio of 2% chord. Figure 2-7 shows the comparison of the iso-vorticity contours for stationary and moving ground boundary conditions. The study also showed that no co-rotating GV, relative to TV, existed for moving ground boundary. The higher strength of counter-rotating SV helped in offsetting the vorticity of TV, which resulted in reduced lift-induced drag compared to the stationary ground boundary.
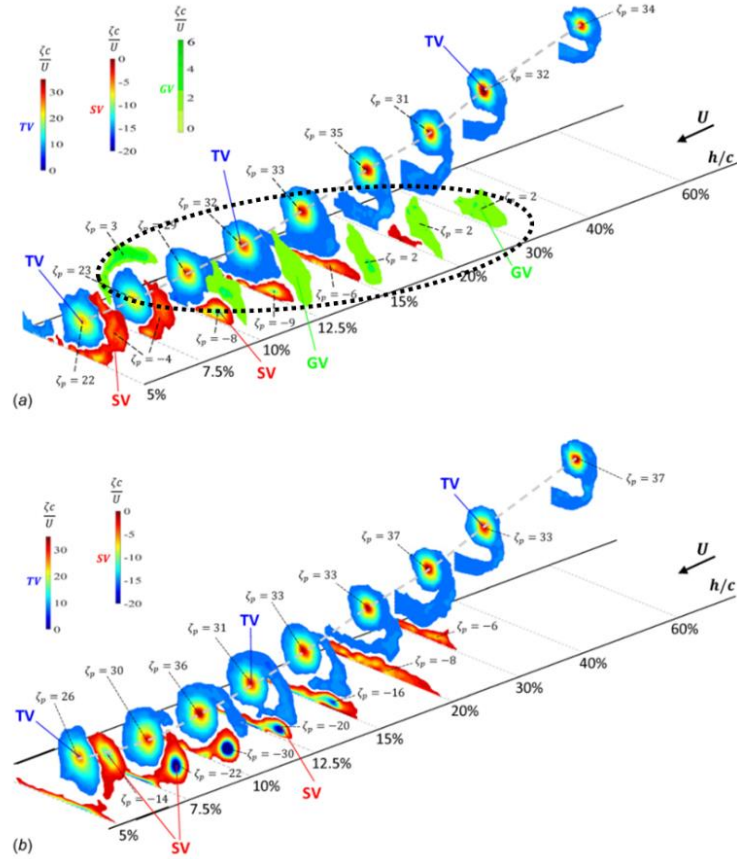
Figure 2-7 Effect of ground boundary conditions on the iso-vorticity contour for (a) stationary ground and (b) moving ground (Lu and Lee (2021))

2.2.2. Ground effect on delta wings and reverse delta wings

Delta wings are generally used in supersonic flights. However, the subsonic flight during take-off and landing unavoidably leads to a large change in ground proximity-produced change in aerodynamic performance. Various attempts have been made to understand its aerodynamic performance in ground effect.

Qu et al. (2015) performed a numerical investigation of a 65°-sweep delta wing in ground effect. The value of the ratio of ground clearance to the central chord of the delta wing was varied from 0.1 to 1.5 at a constant angle of attack $\alpha = 20°$. It has been noted that the variations on the windward

side of the wing contribute to significant changes in aerodynamic forces on the wing and that before the rupture of the leading-edge vortex (LEV) occurs, there is an enhancement in its strength due to the ground effect produced RAM pressure. It was also noted that the ground effect promotes the earlier bursting of LEV. Further, Qin et al. (2018) studied the mutational ground effect on the delta wing (i.e., a ground effect due to abrupt change in height) at $\alpha = 20°$. It was observed that a monotonic elevation (or demotion) was seen in lift, drag, nose-down pitching moment and total aerodynamic forces on the windward side of the delta wing due to a sudden increase (or decrease) in the height of the delta wing above the ground. During landing (or take-off), an increase (or decrease) in the intensity of LEV and an advancement (or delay) in point of LEV breakdown is seen. Lee and Ko (2018) experimentally studied the ground effect on a delta wing. There was an increase in the lift of the delta wing for small angles of attack, which rapidly fell with an increase in the angle of attack and ground distance. The intensity of the LEV was also found to increase, but the ground proximity-induced increase in the adverse pressure gradient (i.e., dp/dx > 0) caused an earlier LEV separation. From the above brief review, it is clear that the delta wing is not suitable for operation in ground effect due to undesirable earlier burst of LEVs and subsequent loss of lift.

The reverse delta wing is a unique type of wing employed in Lippisch-type WIG craft (as discussed in Chapter 1). Musaj and Prince (2008) studied the effect of ground proximity on the aerodynamics of the reverse delta wing with a W-shaped leading edge both numerically and experimentally. The experiment was conducted at Re = 6.9×10^6 and for numerical analysis STAR CCM+ software package was used. The results showed a phenomenal increase in the lift coefficient, and a lift-to-drag ratio of 30 was achieved at a ground distance of 9% span. It was observed that the dynamic air cushion was relatively stable, thereby resolving the problems created by high pressure and low-velocity concentrations. Altaf et al. (2011) used PIV to study the flow pattern and a force balance

to measure lift and drag coefficients of a reverse delta wing in ground effect and compared with the performance of a delta wing formed by reversing the same wing. It was seen that the reverse delta wing had a lower magnitude of tangential velocity and vorticity compared to the regular delta wing at a given angle of attack due to an earlier roll up of the LEVs. With a lower free steam velocity, the circulation of the reverse delta wing was 19% and 33% lower at a spanwise distance of 1.3 times chord and 3.4 times chord, respectively, because of the lesser magnitude of tangential velocity for an earlier rollup. The effects of winglets on the anhedraled reverse delta wing were investigated by Lee and He (2018) at Re = 3.81×10^5. The addition of winglets added two co-rotating vortices, and these vortices proceeded to merge into a single vortex system in the wake region. It was noted that the addition of winglets along with the anhedral provided a significant change in vortex flow properties and also an increase in aerodynamic performance. Lee et al. (2019) performed a study of ground effect on a slender reverse delta wing with 8°, 15°, 22°, 30° and 45° anhedral angles, and then compared the performance of the reverse delta wing with anhedral angles to a baseline wing without any anhedral. It was observed that the lift coefficient increased with the increase in the anhedral angle as the ground was approaching. For an anhedral angle > 30°, C_L started to decrease to a value lower than the value at an anhedral angle of 30°, and C_D increased linearly with respect to C_L as the ground approached. The increase in lift coefficient with lowering ground distance and increasing anhedral angle led to a consistently rising total circulation of vortices of the reverse delta wing. In conclusion, it was noted that vortices of the reverse delta wing moved outwards with increased anhedral and decreased ground proximity. However, this study's main highlight was that adding an anhedral angle decreased the trailing vortex's peak strength. Ko et al. (2020) experimented with inverted delta wing in ground effect at Re = 3.82×10^5. A wing with a 65° sweep angle and a central chord of 35 mm, and a span of 32.64

mm was used for the experiment. They concluded that both lift and drag increased for the reverse delta wing in ground effect. A 145% increase in the lift was obtained at a ground distance ratio of 0.5% chord at a 3° angle of incidence. Due to the ground effect, there was an increase in size and circulation of the reverse delta wing vortex; however, its peak vorticity was reduced.

In conclusion, the reverse delta wing had a lesser magnitude of maximum lift and a delayed stall than its delta wing counterpart. Due to this lower lift, there was a lower drag in the reverse delta wing for the given sweep angle, due to which there was an improved lift-to-drag ratio compared to the delta wing. Hence, the reverse delta wing was more suitable for operation in the ground effect than the delta wing.

Finally, it is worth noting that Jamei et al. (2016) performed a parametric study of a compound wing (Figure 2-8) and compared it with the rectangular wing, both having a NACA 6409 section in ground effect. Even though the compound wing's significant section was rectangular, it had two ends resembling a swept wing. The study's main aim was to understand the change in aerodynamic performance with the change in design parameters (i.e., length of the rectangular span, change in taper ratio, and change in taper angle). The compound wing had eight variants with varying middle span ratio, taper ratio, and anhedral angle, but the root chord length and total wingspan were kept constant to maintain the same airfoil length and AR between the two wings. The simulations were
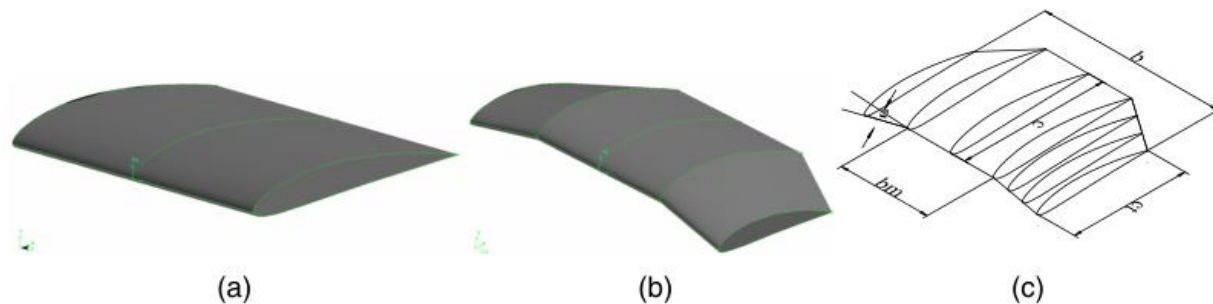
Figure 2-8 (a) Rectangular wing, (b) compound wing, and (c) explanation of compound wing (Jamei et al. (2016)).

done at different ground distances and angles of attack at a constant free stream of 25.5 m/s. The results showed a favourable enhancement of lift-to-drag ratio with changing mid-span of the compound wing. The lift-to-drag ratio change was more rapid with the change in the compound wing's anhedral angle. However, there was a restriction of the maximum anhedral that can be obtained due to the ground's proximity. The compound wing performed better at all conditions below the ground distance ratio < 0.2 of the chord than the rectangular wing. Jamei et al. (2016) further extended the compound wing's parametric study to observe the changes in the aerodynamic coefficient. It was concluded that the span on the side wing, anhedral angle and the taper ratio of the compound wing caused very notable improvements in the aerodynamic coefficients. With the increase in the anhedral angle, there was a considerable rise in C_L and a decrease in lift-induced drag (C_{Di}). This improvement was due to the high ram pressure and outward movement of the low-strength wingtip vortices. The enhancement of the taper ratio of the side wing had a negligible effect on aerodynamic coefficients. The aerodynamic behaviour was substantially improved for small ground clearance ratios (ground clearance to chord ratio < 0.2).

2.2.3. Control of wingtip vortices in ground effect

It has been seen in the above sections that the lift-induced drag in span-dominated ground effect is dependent on the vorticity of the wingtip vortices. By reducing the vortex strength into smaller values, the lift-induced drag of the wing can be decreased. Various techniques can decrease the tip vortex strength, and these techniques can be divided into tip modifications and tip devices. Tip modifications are done by changing the wing tip's shape, including wingtip rounding, sharpening, cutting off, drooping, sweeping and using raked wingtips. Tip devices are the extra attachments such as end plates, winglets, flaps, strakes, and splines added to the tips. Figure 2-9 shows the
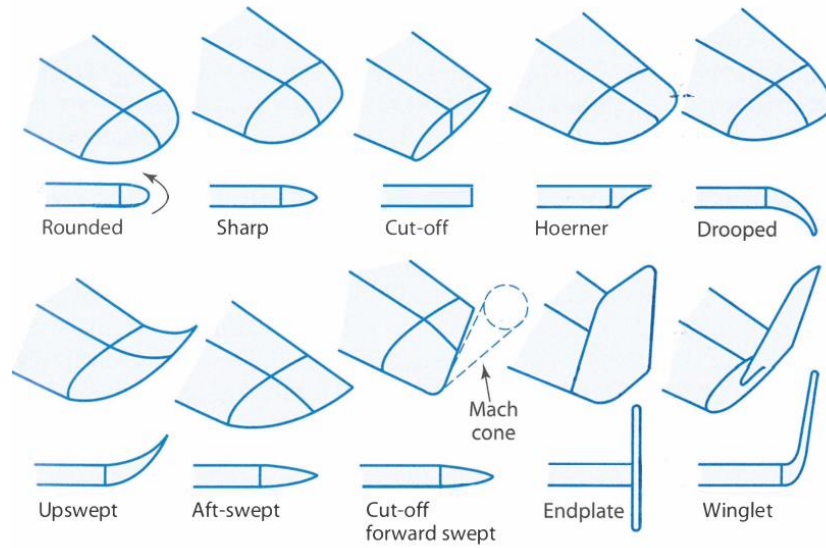
Figure 2-9 Various techniques to reduce wingtip vortices (Raymer (2018))

various techniques used in finite wings that alter vortex structure and roll up. In general, tip attachments are preferred over tip modification because they offer the freedom to improve their shapes for better control. The ideal way of making the wingtip vortices disappear is by making the wing infinite. However, a practically feasible solution to achieve this is to add endplates, but their use is discouraged due to the sizeable wetted area, which increases the profile drag. If the shape of these endplates is streamlined, then there is a reduction in profile drag and wingtip vortices; so-called winglets are nothing but streamlined endplates (Raymer (2018)). The use of winglets and other tip attachments have been discussed below.

A swept wing was taken into consideration by Gerontakos and Lee (2006a) for experimentation in OGE. The swept wing had a NACA 0015 profile at a root chord Re = 1.81×10^5. One of the experiment's main features was the plotting of the spanwise circulation and the calculation of C_L using the spanwise plot of circulation. The experiment covered 80% of the wingspan; the spanwise bound circulation showed a steep decrease near the wingtips. The bound vorticity (Γ_b) was found to be 0.37 times the total circulation (Γ_o). The calculation of C_L from bound circulation was found
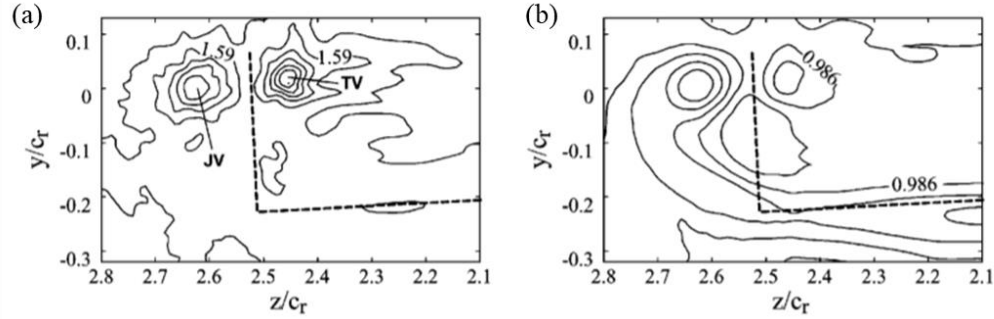
Figure 2-10 Diagram depicting TV and JV with 90° winglet for a swept wing in OGE case (a) iso-vorticity contour (b) iso-axial velocity (Gerontakos and Lee (2006b)) (TV and JV denote trailing vortex and junction vortex respectively)

to be in good agreement with the force balance value. Further, Gerontakos and Lee (2006b) provided proof for reducing wingtip vortices by attaching winglets to the wingtip. They investigated the effect of winglet dihedrals on the tip vortices of the swept wing in OGE. All experimental conditions for this experiment were replicated from the previous experiment (Gerontakos and Lee (2006a)). The winglets were tested at nine dihedral angles (0°, ±20°, ±40°, ±67.5°, ±87.5°) to the main wing. It was noted that the vortex strength of the TV was much lesser than that of the baseline wing. However, due to the joint between the wing and the winglets, there was an extra vortex called junction vortex (JV), as shown in Figure 2-10. It was concluded that the lift-induced drag coefficient (C_{Di}) was permanently reduced due to the addition of winglets and that the negative dihedral angles were more efficient in reducing C_{Di} than the positive dihedral angles.

Sohn and Chang (2012) visualized the flow field of the wingtip vortices by using particle image velocimetry (PIV) for three different wingtip configurations of a swept wing. The swept wing had a root chord length of 257 mm, and the span of the wing was 616.2 mm. The root section of the swept wing was NACA $63_2 - 215$, and the tip section was NACA $63_1 - 212$. The wing configurations were a swept wing with square-cut, a swept wing with simple flaring and a swept
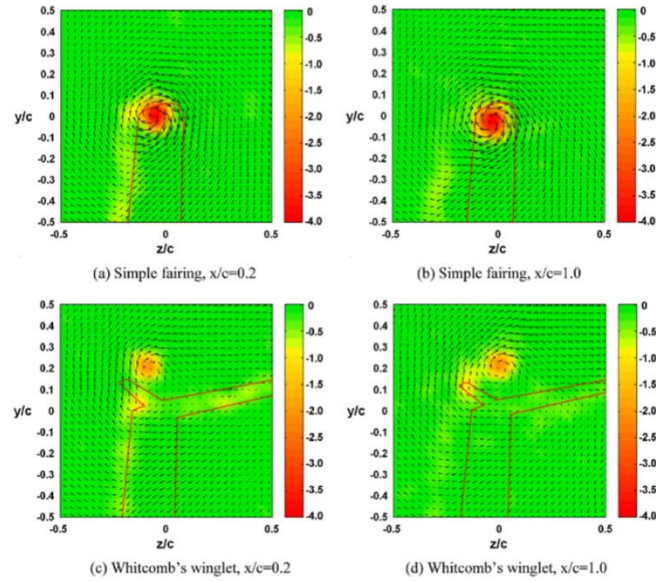
Figure 2-11 Comparison of PIV-measured crossflow velocity and streamwise vorticity for (a) simple fairing and (b) Whitcomb's full winglet ($\alpha = 10°$) (Sohn and Chang (2012)).

wing with a Whitcomb's winglet. Figure 2-11 shows the results obtained by the PIV study. The PIV measurements showed that both the magnitudes of the vw-crossflow velocities and the streamwise vorticity for a Whitcombe's winglet were significantly less. This conclusion proved that attaching a Whitcombe's winglet seems like a more viable option for controlling the vorticities.

Another type of attachment that is useful in decreasing the wingtip vortices is the attachment of a half delta wing to the wingtip. Lee and Pereira (2013) investigated the reduction in wingtip vortex by attaching a slender half delta wing to a NACA 0012 rectangular wing at Re $= 2.81 \times 10^5$. The half delta wingtip attachment could deflect by an angle to the rectangular wing. Figure 2-12 shows the comparison of the iso-vorticity contour between the two. It was concluded that there was an increase in lift coefficient regardless of the value of the angle of deflection of the half delta wingtip attachment. However, the attachment caused an increase in the total drag and both the lift

25
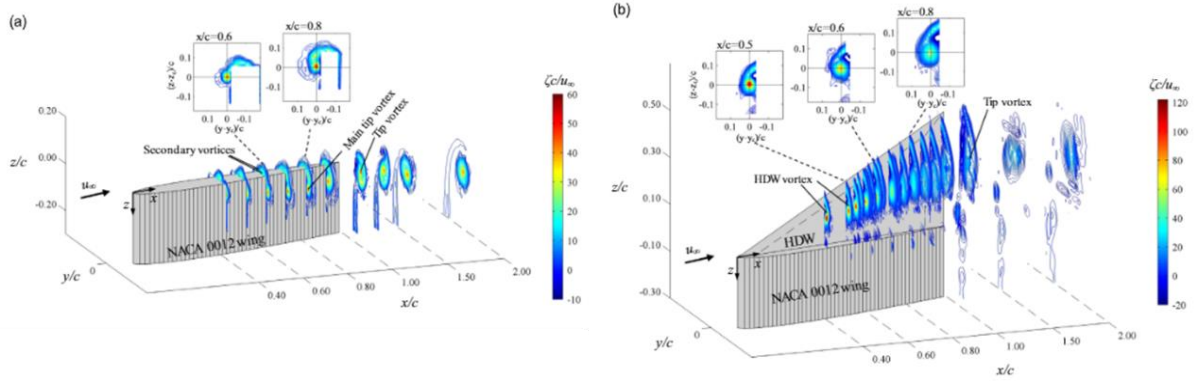
Figure 2-12 Vortex flow structure along the tip and near field of (a) rectangular wing and (b) rectangular wing with half delta wingtip (Lee and Pereira (2013))

coefficient and the drag coefficient also increased with the angle of deflection. For deflection angles, 5° and below the lift-induced drag seemed to decrease with the addition of the half delta wingtip attachment. Meanwhile, for a deflection angle of 10°, the lift-induced drag seemed to increase with the half delta wingtip attachment. It was seen that there was an increased total lift-to-drag ratio due to the addition of the half delta wingtip. One of the critical conclusions of the study was that the presence of half delta wingtip attachment led to a significantly modified roll up of the tip vortex due to the early breakdown of the half delta wing vortex. Further, Lee and Choi (2015) investigated the control of wingtip vortex by attaching tip-mounted half delta wings of different lengths to a NACA 0012 rectangular wing. The length of the half delta wing attachment varied from 0.3 times the chord to the entire length of the chord of the rectangular wing. It was seen that the 0.5 times chord half delta wing attachment gave the most reduction in lift-induced drag.

Narayan and John (2016) conducted a numerical study to investigate the effect of wingtip vortices created by attaching various winglets in a subsonic flow regime. A swept wing model was used for the study and had a NACA 2421 airfoil cross-section with a span of 3 m and a root chord of 0.25 m. The simulation was performed in ANSYS FLUENT software package, and the k–ω SST model

26
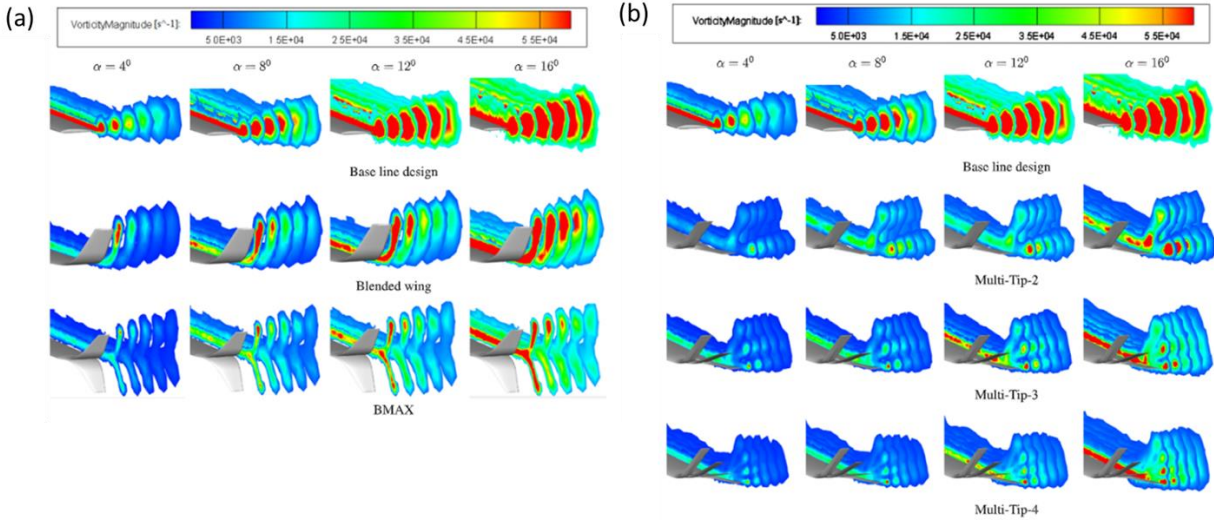
Figure 2-13 Vorticity contours at various α for (a) baseline wing, blended and BMAX winglet designs, and (b) multi-tipped winglet designs (Narayan and John (2016)).

was used at Re = 7×10^5. Two different winglets were simulated, and their performance was compared with the baseline wing. The vorticity contours obtained are shown in Figure 2-13. The results concluded that the BMAX winglet outperformed the blended winglet. The BMAX winglet had an aerodynamic efficiency of 14%, and the blended winglet had an aerodynamic efficiency of 3.5% compared to the baseline wing. When it came to the multi-tip winglet, the multi-tip winglet 3 with three split vortices had an aerodynamic efficiency increase of 22.5%, which proved that it is a better arrangement among all the other techniques. Deshpande et al. (2021) investigated the feasibility of attaching winglets to a fixed-wing mini unmanned aerial vehicle (UAV) to increase its aerodynamic efficacy and flight endurance. The experiment was conducted with a UAV model in a low-speed wind tunnel with a PIV setup to measure the flow field changes. The UAV had a swept wing configuration with a sweep angle of 9.48° and an aspect ratio (AR) of 6.56. Flow diagnostics revealed strong vortices present without the winglets, but the winglets significantly diffused the strength of the tip vortices. Due to loss of strength in the tip vortices, the C_D reduced by 7.5% at an angle of attack of 0°, which indicated that the UAV was more efficient for straight

and levelled fights due to the introduction of the winglets. A 15% increase in flight endurance was achieved due to the reduced power consumption of the UAV. Based on the actual fight test conducted for the UAV, it was noted that the aerodynamic efficacy was increased by 10%–12%. It was concluded that a winglet design optimization was required to increase the efficiency of the UAV further. From the above investigations, it can be concluded that the reduction of wingtip vortex strength by splitting into many vortices with lesser vorticity is an efficient means of wingtip vortex control in the OGE case.

On the other hand, the ground effect on the investigation on formation, growth and development of wingtip vortices is minimal. As per the author's knowledge, no literature is available on wingtip vortex control using winglets for swept wings in ground effect. Hence all other tip attachments that researchers have investigated have been given below. Zhang and Zerihan (2004) studied the flow structure of the wingtip vortices developed by an inverted double-element wing in ground effect with end plates attached on the ends. The experiment was conducted in a wind tunnel with varying ground distances. The purpose of this double element wing was to produce sufficient downforce when it is attached as a flap behind a race car. It was found that there was a three-dimensional flow for the main element of the flap near the wingtip. However, the downforce was less significant at the tips due to reductions in the tip vorticity because of the introduction of the endplates. A total downforce versus ground distance graph was plotted for both high and low flap angles. There was an initial rise in downforce in both cases due to concentrated edge vortices followed by force enhancement and vortex breakdown. Finally, there was a loss of downforce due to separation noticed on the wing. The edge vortex was responsible for the region of high suction near the tips of the two elements. When the strength of this edge vortex was high, the downforce produced by the flap was large, and after vortex breakdown, there was a tremendous loss in

downforce. The study also indicated the effect of endplates on the tip vortices; due to the endplates that were essential to support the two elements on the flap, the formation of the vortex shifted from the tips to the edges. Galoul and Barber (2007) used laser doppler anemometry to study the downforce generated by an inverted wing with endplates in a wind tunnel with a moving belt below it. The wing had a NACA 4412 profile, and the experiment was conducted at a chord based Re = 50,000 with varying ground distances. The use of endplates introduced two co-rotating vortices, one at the top and one at the bottom of the endplate. It was observed that the two vortices are different in nature, and the lower vortex was more potent than the upper one, and it changed the trajectory of the upper vortex. Even though there was an initial split in the vortices due to the introduction of the endplate, vortex merging occurred within two chord lengths downstream of the wing.

Lee et al. (2010) numerically investigated the aerodynamic characteristics and stability of a plane wing, a wing with an endplate and a wing with an anhedral angle in ground effect. Due to the introduction of the endplate, the high-pressure air cannot escape from the gap between the wing, which increased the lift of the wing for a slight increase in drag. Due to this, there was an increase in the lift-to-drag ratio and the magnitude of the tip vortex was reduced. The endplate split the wingtip vortex into two lower strength vortices and these two vortices decayed in magnitude reasonably close to the wing along the downstream distance. This was a significant reason for the decrease in the lift-induced drag for the wing with the endplate. With decreasing ground proximity, the plain wing had an intermediate decrease in lift-induced drag, and this mainly occurred due to a lack of space for vortex development. A stagnation point moving upward was seen for the wing with anhedral due to which there was an increase in pressure drag with the decrease in ground proximity. Even though the leading edge area was minimal, it had a significant contribution

29

towards variations in drag. The leading edge pressure drag in the anhedraled wing seems to nullify the drag reduction due to ground proximity. This study concluded that the use of anhedraled wing with endplates was predicted to improve the lift-to-drag ratio further and increase the wing's stability in ground effect.

Lu and Lee (2020) experimented with the passive method to control wingtip vortices by attaching a semi-half delta wing, and a semi-half reversed delta wing to a NACA 0012 rectangular wingtip in ground effect. They experimented with 50° and 65° sweep angles for the wingtip attachment, and experiments were conducted at a Re = 2.81×10^5. The rectangular wing had a chord = 28 cm and semi-span = 50.8 cm, and an aluminum plate replicated the stationary ground boundary condition. The wingtip arrangement used for experimentation is shown in Figure 2-14. Drastic
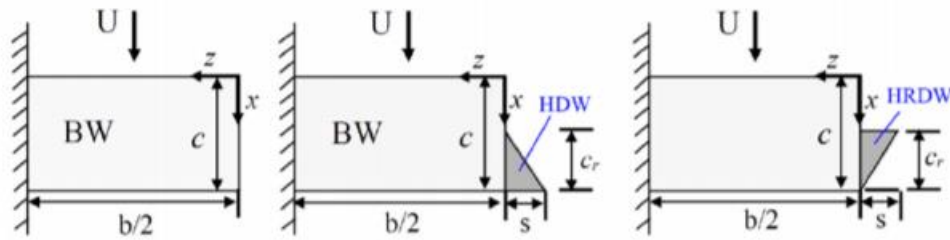
Figure 2-14 Half delta wing (HDW) and half reverse delta wing (HRDW) attached to a rectangular wingtip (Lu and Lee (2020))

changes in the characteristics of the tip vortex were seen due to the introduction of tip-mounted half delta wing and half reverse delta wing attachments. It was noted that the peak vorticity for tip-mounted 50° half reverse delta wing was the least in all cases of ground proximity and caused the most significant reduction in the critical vortex flow properties and caused the highest increase in aerodynamic efficiency.

Zhou et al. (2020) experimentally investigated the ground effect on a NACA 4412 wing with two types of tip-sails, namely long and short. Time-resolved particle image velocimetry was used to

observe the flow structure of the tip vortices, and force balance was used to measure the lift and drag coefficients with a varying ground distance between 15% chord to 100% chord. There was an elevated lift-to-drag ratio due to the ground effect than the tip sails because the tip sails' primary function was to reduce lift-induced drag by lowering the strength of tip vortices. Due to the introduction of sails, there was an increase in the wing's effective aspect ratio, thereby increasing the lift coefficient compared to the bare wing. The short sails, which had a length of 25% chord, were more useful in drag reduction than the long sails, which had a length of 35% chord. The tip-sails quickened the dissipation of the tip vortices, the effect of drag reduction by tip-sails gradually enhanced with the increase of the angle of attack.

Based on the above literature for the OGE case with winglets and other attachments in the IGE, it was concluded that since there is an effective reduction in peak vorticity for the OGE case by introducing winglets, there should also be a reduction in peak vorticity for the IGE case by winglet attachments.

2.3. Summary of literature review

From sections 2.1 and 2.2 of the literature, it was clear that there was a significant difference in the performance of the cambered airfoil and symmetric airfoil at very close ground proximity. At extreme ground proximity, the symmetric airfoils experienced a converging-diverging effect due to the convex shape of the lower surface of the airfoil. Due to this effect, the C_l of the symmetric airfoil became negative at low angles of attack because of the flow blockage created. Also, based on sections 2.1 and 2.2, it was clear that the ground effect on the swept wing was span-dominated and not chord-dominated. Due to this point, it was concluded that no further experimentation was required on the NACA 0015 symmetric airfoil, which was the profile of the swept wing used in experimentation.

The investigations done in sections 2.1 and 2.2, on the discrepancies created due to the variations in the surface boundary conditions showed that for a stationary ground boundary, at the ground distance ratios below 15% of chord, there was an existence of ground vortex, which was created due to the roll up of the longitudinal boundary layer. This ground vortex caused an acceleration of the flow at the lower surface of the 2-D airfoil and the 3-D wing, due to which a reduced value of lift coefficient was seen for the fixed ground boundary compared to its moving ground boundary counterpart. Hence it was decided that moving ground boundary was better suited for experimentation in ground effect. However, due to experimental limitations of the wind tunnel, a stationary flat plate with a large elliptical leading edge to reduce the impact of ground boundary conditions was used for experimentation.

The span-dominated ground effect on the swept wing was closer in nature to the span-dominated ground effect of the rectangular wing. This was because both the rectangular wing and the swept wing had free end effects and fell under the category of finite wings, as studied in section 2.2. On the contrary, the ground effect on delta wings and reverse delta wings did not fall under the category of span-dominated ground effect. The most important observation from section 2.2 was that the delta wing was unsuitable for ground effect due to the loss of lift created by ground effect promoted LEV burst of the wing. Even though the reverse delta wing had superior aerodynamic properties and flow patterns than other wings, it was thoroughly researched previously by Ko. (2017). It was also essential to note that all performance augmentation techniques for the reverse delta wing, which included providing anhedral (studied by Lee et al. (2018)), providing winglets (studied by Lee and He (2018)), and changing the leading edge (studied by Musaj and Prince (2008)), were studied by other researchers. Hence the swept wing was considered for experimentation.

Wingtip vortices only appear in the case of span-dominated ground effect as the outward movement of these vortices produces the ground effect. The control of wingtip vortices in both IGE and OGE cases was discussed in section 2.2. In the OGE case, two types of wing attachments were studied for wingtip vortex control: variable length half delta wing attachments and multiple variations of winglet attachments. The winglets helped in the dispersion of the vortex strength of the TV into smaller vortices, and therefore, wings with winglets showed a better performance in OGE (Gerontakos and Lee (2006b)). Furthermore, the half delta wing attached to the end of the rectangular wing showed the most reduction in tip vorticity (Lee and Choi (2015)). Hence both the above attachments seemed to decrease the strength of wingtip vortices. In the IGE case, several attachments have been discussed for wingtip vortex control. These attachments included the use of endplates, delta wing attachments, tip sails and winglets. However, since the endplates increased the drag due to their blunt shape, the use of tip sails was discussed by Zhou et al. (2020) and, the use of half delta wing and the reverse delta wing as wingtip attachments was already done by Lu and Lee (2020), the attachment of winglet seemed to be the more viable option. The above points provided confidence to study the swept wing in the IGE case using winglets. Since the swept wing's geometry resembled the wing used by Gerontakos and Lee (2006b), the same winglet configurations and experimental conditions used in their study for the OGE cased were considered sufficient and easy to replicate aerodynamic study of the swept wing in the IGE case. As a conclusion of this summarization of the literature review, the following objectives were realized as necessary and sufficient to study the near wake of the swept wing in ground effect.

2.4. Objectives of the current research

This research work aims to investigate the ground effect on the vortex flow structure generated behind a NACA 0015 swept and tapered wing with winglets of different configurations in the

subsonic wind tunnel in the Department of Mechanical Engineering at McGill University. The vortex flow characteristics at various ground distances at a fixed downstream distance are obtained by a miniature seven-hole pressure probe. These wake flow measurements will be used to quantify the impact of the ground proximity and winglet attachment on the circulation and rotation speed and trajectory of the vortex. Special emphasis is placed on the evolution of the vortex flow system along the streamwise distance at two fixed ground distances. Further, importance is given to understating the change in vortex flow structure due to the introduction of winglet attachments to the end of the wingtip in ground effect. The vortex flow of the baseline wing (i.e., the swept wing with no winglet) is also measured to serve as a comparison. The measured vorticity flow field will also be used to quantify the impact of winglets on the change in lift-induced drag in ground effect. The circulation of the vortex will also be used to estimate the lift coefficient.

3. Experimental Methods and Apparatus

This chapter explains the flow facility, wing model, test procedures and parameters, and the data acquisition system and data processing.

3.1. Flow facility

The experimentation took place in Joseph Armand Bombardier wind tunnel in the aerodynamics laboratory in the Department of Mechanical Engineering of McGill University. The wind tunnel is a suction-type wind tunnel and has four sections: the contraction section, the test section, the
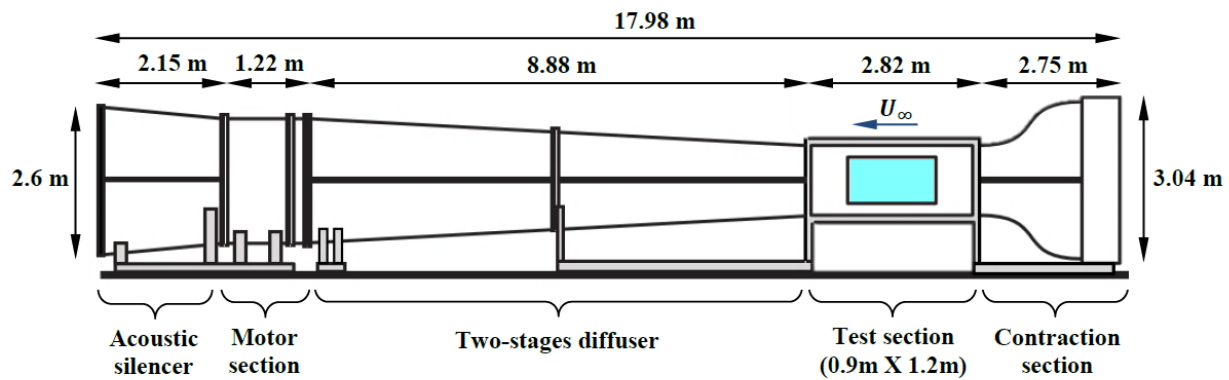
Figure 3-1 Schematic diagram Joseph Armand Bombardier wind tunnel

diffuser section, and the power section (Figure 3-1). The contraction section has a contraction ratio of 10:1. The settling chamber has a honeycomb straightener, which is 10 cm in thickness and has four anti-turbulence screens that are 2 mm thick to minimize the free stream turbulence intensity. The free stream turbulence intensity is 0.05% at 35 m/s. The test section has a 1.2 m width, 0.9 m height and 2.7 m length. The test section is followed by a diffuser section, which is 9 m long. The
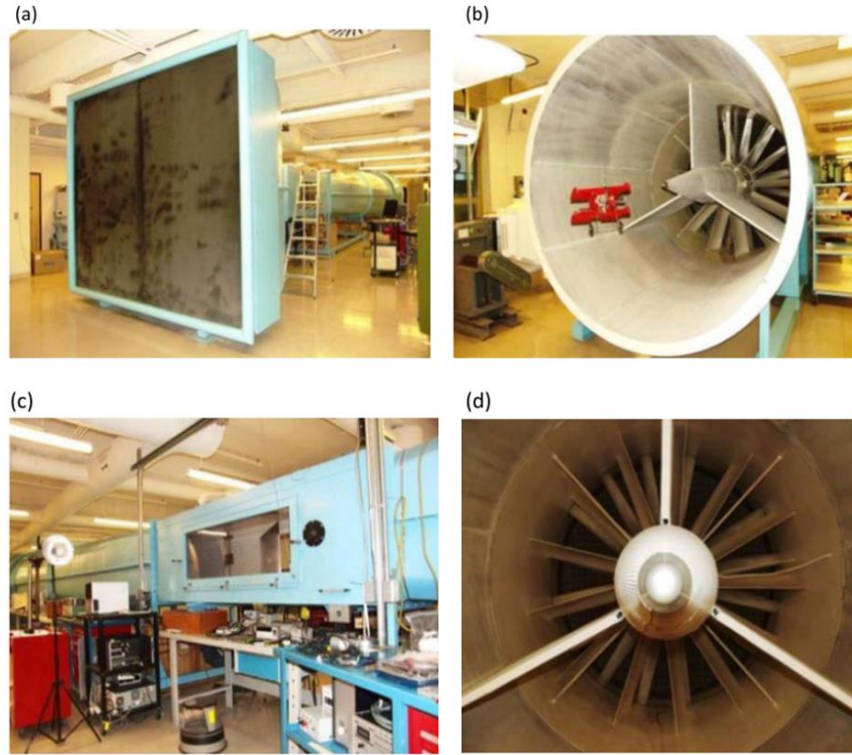
Figure 3-2 Photos of the wind tunnel. (a) The inlet, (b) the exit, (c) the outside of the test section, and (d) zoomed-in view of the exit of the tunnel

wind tunnel ends with the power section, which consists of a 16 – blade fan with a diameter of 2.5 m. This fan provides free stream air, and an AC motor controls its speed, and the motor's sound is muffled by an acoustic silencer (Figure 3-2). A Honeywell DRAL 501-DN differential pressure transducer connected through a pitot tube was used to measure the flow rate of the free stream, and it had a maximum water head of 50 mm. The transducer had a linear response with a limit of 1%, and the resolution was 97 Pa/V. It was calibrated using a water column of 50 mm.

3.2. Wing model

The wing model used in this experiment was a swept-back tapered semi–wing which had a NACA 0015 profile. The semi-wing model had a root chord of 20.32 cm and a taper ratio of 0.375. Further details of the wing and the winglet are given in Table 1. The wing was fabricated in a CNC machine and had geometrical tolerance of 250 μm. The origin of the coordinate system was located at the

trailing edge of the root chord of the wing with x as streamwise distance, y as vertical distance and z as spanwise distance. The NACA 0015 profile was chosen since previous experiments were done on the same wing in OGE. An elevated flat plate simulated the stationary ground required for experimentation, and the semi-wing was mounted horizontally above the plate, rendering a root chord Re of 1.81×10^5.

Table 1 Geometrical properties of swept and tapered wing and winglet

Wing		Winglet	
Parameter	Value	Parameter	Value
c_r	20.32 cm	c_{wr}	7.62 cm
c_t	7.62 cm	c_{wt}	3.95 cm
$b_{c/4}$	55.88 cm	$b_{c/4}$	7.62 cm
b	51.05 cm	b	6.24 cm
Λ_{LE}	26.9°	Λ_{LE}	40.27°
$\Lambda_{c/4}$	24°	$\Lambda_{c/4}$	35°
Λ_{TE}	14.5°	Λ_{TE}	14.52°
S	713.15 cm^2	S	36.10 cm^2
AR	3.654	AR	1.079
λ	0.375	λ	0.518

The elevated flat plate was made of aluminum and had 1.4 m, 1.2 m, and 2.5 mm as its length, width, and thickness. The wind tunnel boundary layer effects were overcome by placing the flat plate 15 cm above the tunnel wall. An elliptical profile was adopted at the leading edge of the flat

	x/c_t	x/c_r
	-0.066	0.625
	0.934	1.0
	2.267	1.5
	3.601	2.0
	5.601	2.75
	7.601	3.5
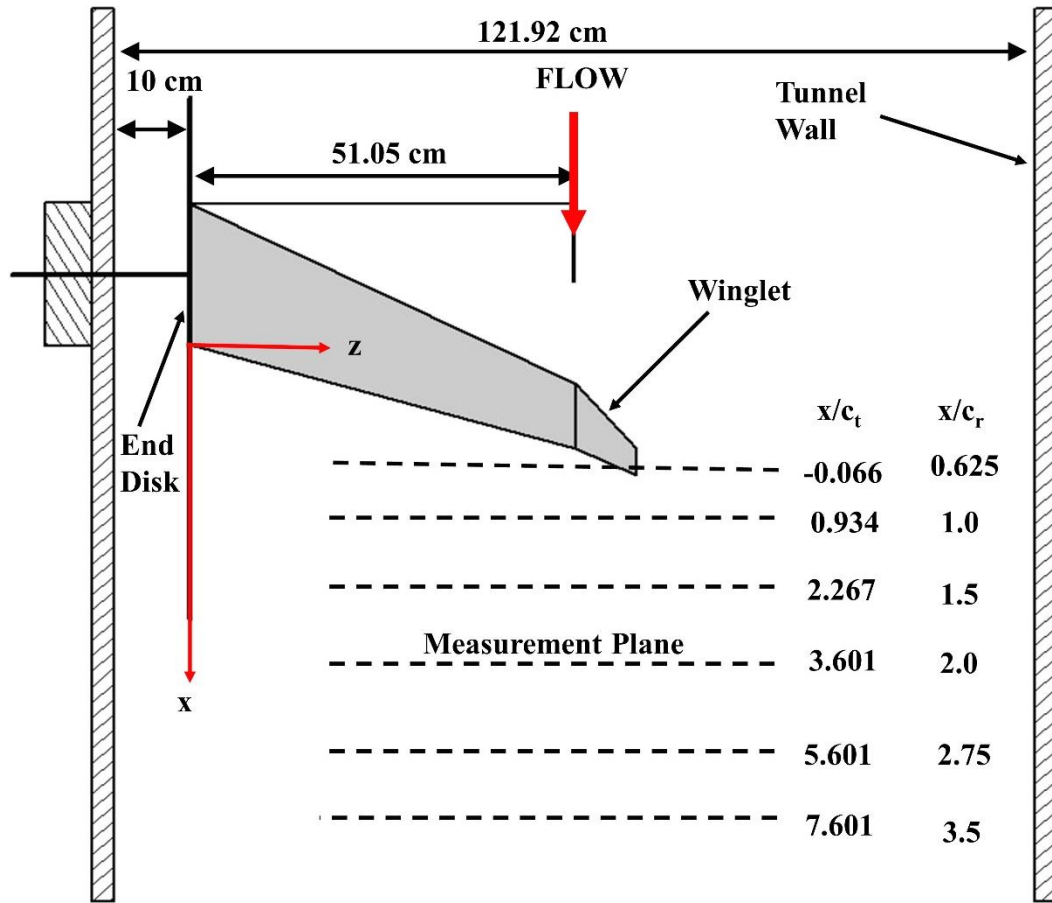
Figure 3-3 Schematics of wing model with co-ordinate system

plate, and the major to minor axis ratio of the ellipse was maintained at 5:1. The distance between the wing's trailing edge and the ground's surface was taken as h and was referred to as ground distance. The ground distance ratio was obtained by dividing the ground distance by the root chord (h/c_r). In the present experiment, the ground ratio changed from 60% to 5%. Figure 3-3 depicts the schematics of the wing model.

The winglet was attached and removed based on the need of the experiment. The winglet was 3-D printed using ABS as the material. It had a root chord length that matched the tip chord length of the swept wing, which was 7.62 cm. The taper ratio of the winglet was 0.518, which was higher than the swept wing, had a span of 6.24 cm. The winglet was designed with two deflection angles,

38

45° and 90°, relative to the swept wing. It is important to note that when the winglet was at 90° to the swept wing, it did not change the AR of the swept wing. However, when it was at an angle of 45°, the AR of the swept wing increased by 17.9%. The span of the winglet times the cosine of the deflection angle was added to the AR of the swept wing.

3.3. Seven-hole pressure probe

The three mean pointwise velocity components (u,v,w) were measured by the use of a miniature seven-hole pressure probe, as shown in Figure 3-4. The probe has three main parts, the probe tip, the probe shaft, and the probe sting. The probe's tip had a maximum outer diameter of 2.8 mm; it
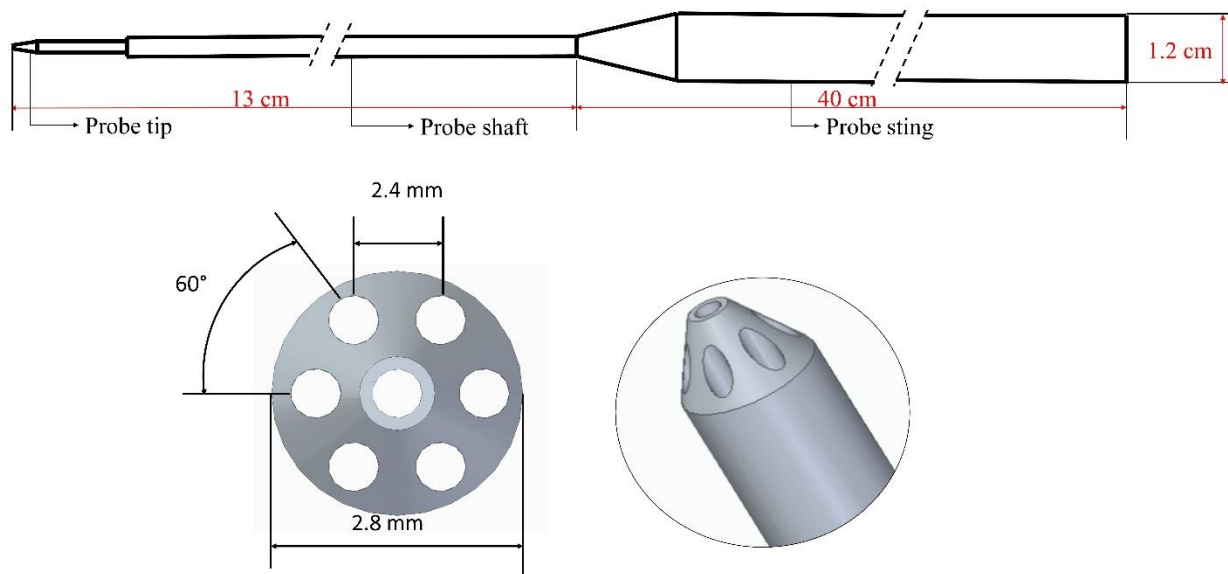
Figure 3-4 Schematic of seven-hole pressure probe

had a conical tip with a tip angle of 30° and was made from brass. The tip also had seven holes drilled into it, one on the centre and the other six on the cone's lateral surface at 2.4 mm. The length of the probe sting was 400 mm, and it had a diameter of 12 mm. Tygon tubing was used inside the probe sting to allow the flow to reach the pressure transducers, and it had a diameter of 1.6 mm and a length of 550 mm which was connected to transducer assembly box. The assembly box had

seven Honeywell DC002NDR5 differential pressure transducers, and their maximum pressure head was 50 mm of water. A signal conditioner was built in-house to filter the signal, and then a differential amplifier amplified it with a gain ratio of 5:1. The transducers had a linear response of 2% and an average resolution of 61 Pa/V.

The movement of the seven-hole pressure probe was done by using a custom-built traverse mechanism with two-degree of freedom in the yz plane, as shown in Figure 3-5. The movement in y and z directions was controlled by Labview NI PCI-7344 4-axis motion controller and was in conjunction with the data acquisition. The fixing of streamwise position x was done manually by setting the traverse mechanism at the desired position in the near wake.
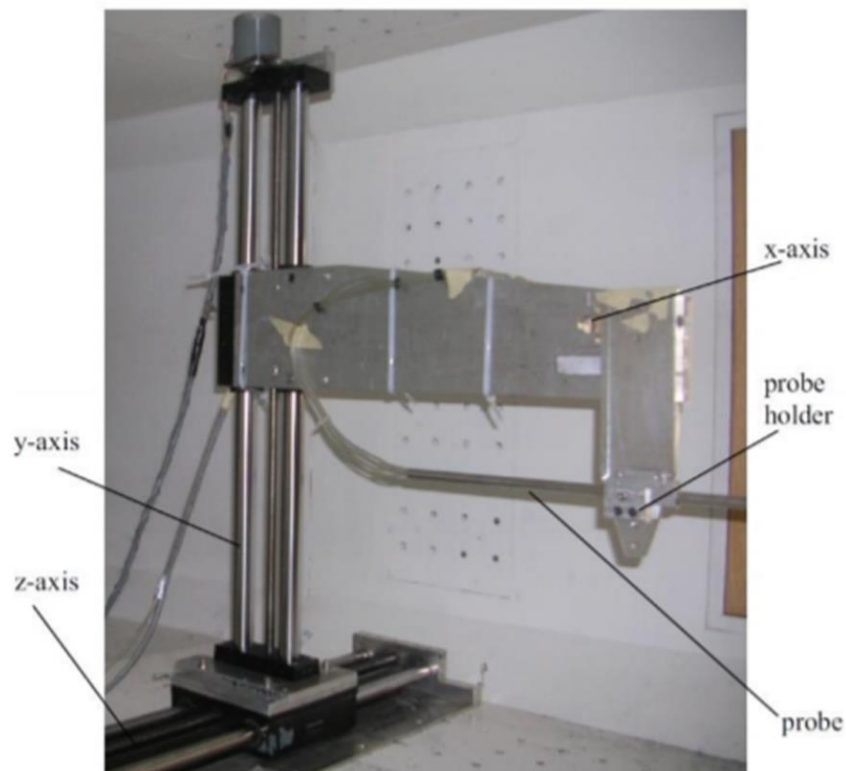
Figure 3-5 Traverse mechanism assembly

3.4. Data acquisition and analysis

A 16-bit and 16 channel NI-6259 A/D board, run by a Dell Dimension E100 PC, was used to get the data required from the seven-hole pressure probe. A NI BNC -2110 connector box was used to link the sensors to the A/D board. Based on the calibration curves, only voltages were recorded and processed for data. The vw-crossflow measurements were obtained as an output downstream of the wing's leading edge at various downstream distances. The spacing between the grids Δy and Δz were set at was one-eighth of an inch or 0.3175 cm. MATLAB program created the grid required for experimentation, and automatic scanning of data points was done by the lab's computer based on that loaded grid. The output voltage sampling was done at 200 Hz for every grid point and a time interval of 5 seconds to increase the output values' reliability for velocities.

The vorticity based on v and w components was obtained as given below,

$$\zeta_{ij} = - \left[\frac{\partial v}{\partial z} - \frac{\partial w}{\partial y} \right] \approx - \left[\frac{v_{j+1,i} - v_{j-1,i}}{2\Delta z} - \frac{w_{j,i+1} - w_{j,i-1}}{2\Delta y} \right] \tag{3.1}$$

Where, $i = 1, 2, 3 \dots m$ and $j = 1, 2, 3 \dots n$. m and n are the numbers of measurement points in the z and y directions, respectively. The above central differencing scheme was used for all the interior node points, and the backward and forward differences were used for endpoints to measure values on the grid.

Stoke's theorem was used to calculate circulation, and this was done by numerical integration of product and vorticity and area. The core and outer circulation were calculated by the formulas given below.

$$\Gamma_c = \sum_{i}^{n} \sum_{j}^{m} \zeta_{i,j} \, \Delta y \Delta z \qquad\qquad r_{i,j} < r_c \tag{3.2}$$

$$\Gamma_o = \sum_{i}^{n} \sum_{j}^{m} \zeta_{i,j} \, \Delta y \Delta z \qquad\qquad r_{i,j} < r_o \qquad\qquad (3.3)$$

Where,

$$r_{i,j} = \left(z_j - z_c\right)^2 + \left(y_j - y_c\right)^2 \qquad\qquad (3.4)$$

$$r_o = r\left(\zeta = 0.001\zeta_{i,jmax}\right) \qquad\qquad (3.5)$$

The origin of the polar coordinate system was set to the vortex center (z_c, y_c). The vortex center was identified as the location with maximum vorticity, and r_c represented the vortex core radius at a point where tangential velocity was maximum. The calculation of tangential velocity (v_θ) was done by the following formula:

$$v_\theta = \left(v_{i,j} - v_c\right)\sin\theta - \left(w_{ij} - w_c\right)\cos\theta \qquad\qquad (3.6)$$

θ represents the polar angle relative to the vortex center. All the numerical and graphical analysis was carried out with MATLAB programs and MS EXCEL spreadsheets.

3.5. Experimental uncertainty

The uncertainties in measurement were based on the uncertainty of measurement in the seven-hole pressure probe and uncertainty in the data acquisition and calculations. Parameters including vortex center location, core radius, streamwise, vertical, horizontal, tangential velocities, vorticity, circulation, and coefficient of lift-induced drag were considered for uncertainty analysis. A jitter program was used to determine the uncertainty in measuring these parameters (Moffat (1982)).

The uncertainties included in the measurements done by the seven-hole pressure probe are given in Table 2, and the explanation is given in the notes below.

Table 2 Uncertainty of seven-hole pressure probe measurement parameters

Quantity	Uncertainty	%	Notes
Position Measurement			
Angular position	±0.0º	0.20	
Traverse y position	±0.254 mm	0.09	
Traverse z position	±0.762 mm	0.27	
Traverse x position	±0.254 mm	0.09	
Maximum Normalization Uncertainty:		0.36	1.
Grid resolution			
y coordinate (spanwise)	±3.175 mm	1.14	
z coordinate (traverse)	±3.175 mm	1.14	
Total Uncertainty in vortex center location:			2.
y coordinate	±3.241 mm	1.16	
z coordinate	±3.325 mm	1.19	
Total Uncertainty in vortex radius:	±2.319 mm	0.83	3.
Equipment parameters			
Free-stream velocity (14 m/s)	± 0.05 m/s	0.29	4.
Free-stream turbulence intensity (35 m/s)	± 1.75 m/s	0.05	5.
Model profile (8" NACA 0015)	± 0.06 mm	0.03	6.
Maximum Normalization Uncertainty		**0.30**	1.

Probe Measurement			
Reference pressure		0.13	
Transducer accuracy		0.25	7.
Transducer sensitivity	±0.032 mm H_2O	0.18	8.
Transducer calibration (linearity)		0.02	8.

The uncertainties due to data acquisition and calculation are given in Table 3, and the explanation is given in the notes below.

Table 3 Uncertainty in data acquisition and calculation

Quantity	Uncertainty	%	Notes
Signal Processing			
Amplifier reference voltage		0.05	
A/D Conversion			
16-bit A/D conversion of 3.5V signal	±1 mV	0.02	9.
Total Pressure Uncertainty:	±0.06 mm H_2O	0.34	1.
Data Reduction			
2nd order calibration grid interpolation		1.46	10.
Filtering		0.5	11.
Total Data Reduction Uncertainty:		**1.54**	1.
Total Uncertainty in Velocity Fields:			
u velocity	±0.475 m/s	2.8	12.
v velocity	±0.254 m/s	1.5	12.

w velocity	±0.254 m/s	1.5	12.
v_θ velocity	±0.359 m/s	2.1	13.
Vorticity Calculation			
2nd order finite differences	±0.762 Hz	3.85	14.
Uncertainty in Vorticity Field		8.21	15.
Total Uncertainty in Vorticity Field:		**9.07**	1.
Total Uncertainty in Circulation:		**11.14**	16.

Notes:

1. Using a constant odds combination by Moffat (1982).

2. Constant odds combination of grid, angular position and traverse position has been used to determine the uncertainty in the total vortex center.

3. The uncertainty is the total vortex core radius is determined by using the combination of y and z with the help of the constant odds combination. Therefore, the core radius and the outer radius have the same uncertainty since the same parameters determine the vortex's core and outer radius.

4. Method published by Barlow et al. (1999) has been used to measure the uncertainty in the measurement of velocity using the pitot tube.

5. Uncertainty in the measurement of the free stream by the hot-wire anemometer.

6. The process of manufacturing the wing gives the value of tolerance.

7. As specified by the manufacturer specifications.

8. Measured from the calibration done for pressure transducer and transducer sensitivity. Details of the analysis are as follows:

- Transducer sensitivity (rated): ±5 mV.

- The linearity of calibration curve-fit: 99.8%.

- Calibration sensitivity (worst-case scenario): 62.2 Pa/V.

9. Uncertainty was obtained from the standard deviation of instantaneous readings taken from a 3.5 V input at a sampling frequency of 500 Hz over 10 s.

10. It was calculated from a sample calibration data set from the average difference between adjacent measurement points.

11. It was determined from the average difference found in using a 25-pt Gaussian smoothing field.

12. It was determined using the jitter approach with data reduction uncertainty, pressure uncertainty and normalization uncertainty as variables.

13. Total tangential velocity uncertainty is determined using constant odds combination of v and w velocity uncertainties.

14. It was taken as the average error incurred while using the 2nd order finite differences scheme instead of integration or cubic spline curve-fitting.

15. It was determined using the jitter approach (Moffat (1982)) with velocity field (v and w) and positional (y and z) uncertainties as variables.

16. It was determined using the jitter approach with vorticity field, vortex center and core radius uncertainty as variables.

4. Results and Discussions

The ground effect on iso-$\zeta c_r/U$ (vorticity) contour and iso-u/U (axial velocity) contour of the baseline swept wing at $x/c_r = 2$ and $\alpha = 8°$ are presented in section 4.1. In section 4.2, the streamwise progression of the vortex system at $h/c_r = 0.15$ and $h/c_r = 0.05$ for the baseline wing is discussed. Section 4.3 compares iso-$\zeta c_r/U$ and iso-u/U between baseline wing and wing with 45° and 90° winglets. Further, in section 4.4, vortex flow properties are explained. Finally, in sections 4.5 and 4.6, the calculation of C_{Di} and the method of estimation of C_L are described.

4.1. Ground effect on iso-$\zeta c_r/U$ and iso-u/U contours for baseline swept wing

Figure 4-1 shows the impact of ground proximity on iso-$\zeta c_r/U$ contours for $h/c_r = 0.6$ to 0.05 at $x/c_r = 2$. The wing is represented by the (▬▬) green line shown in Figure 4-1, and its corresponding y-axis (h/c_r) value represents the ground distance ratio of the wing. The vorticity ζ ($= \partial w/\partial y - \partial v/\partial z$) calculations are done using a central differencing scheme on vw-crossflow measurements, and the value of ζ_{peak} ($=\zeta_{peak}/c_r U$) is shown by the red dashed arrows in Figure 4-1. Besides the presence of TV, the results also show the presence of counter-rotating SV and co-rotating GV. GV starts to appear at a ground proximity $h/c_r \leq 0.2$, and SV starts to appear at ground proximity of $h/c_r \leq 0.1$ at $x/c_r = 2$. The co-rotating GV adds to the TV and increases overall circulation, and the counter-rotating SV negates the strength of the TV. The TV remains concentrated and moves away from the wing's tip as the wing approaches closer to the ground, as shown in Figure 4-1 (a)-(f). The dashed (▬ ▬) red line denotes the spanwise movement of the TV center, which happens due to a lack of space for vortex development. The shape iso-$\zeta c_r/U$ contours remain unchanged for $h/c_r = 0.6$ and $h/c_r = 0.4$ except for a slight reduction in the strength

47
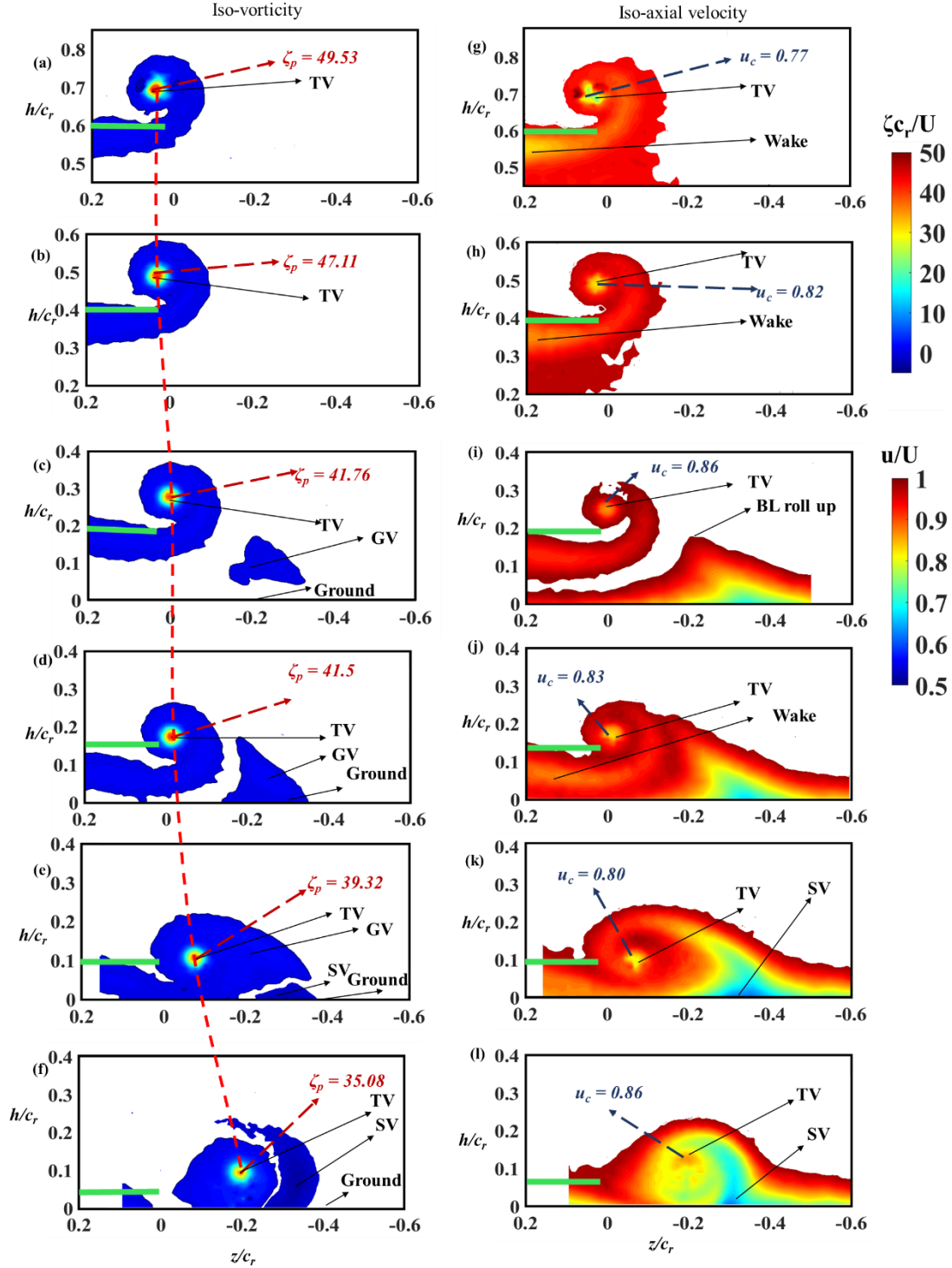
Figure 4-1 Non dimensional (a) -(f) iso-vorticity contours and (g) -(l) iso-axial velocity at $x/c_r = 2$ (The meaning of the coloured lines and arrows is given in the text)

of ζ_{peak} and a minor change in the variation of the center of the TV. This is because the ground

effect felt at these ground distances is minimal. However, there is a considerable reduction in ζ_{peak}

48

at $h/c_r = 0.2$ as the wing is very close to the ground. It can also be noted that at $h/c_r = 0.2$, GV starts to appear, which means that the longitudinal boundary layer has already rolled up. At $h/c_r = 0.15$, GV is quite large and adds to the TV; hence an increase in ζ_{peak} is seen. With the streamwise motion of the two vortices, the GV mergers with TV, and they propagate further as a single vortex system. At $h/c_r = 0.1$, the spanwise boundary layer on the flat plate (ground) has already rolled up and has given rise to SV, which negates the circulation of TV. At $h/c_r = 0.05$, SV's strength is significant, and a higher decrease in ζ_{peak} of TV is seen. Figure 4-1 (g)-(l) also shows iso-u/U contours for the ground effect on the baseline wing at $x/c_r = 2$, and the dashed dark blue arrows give the core velocity. Like iso-ζc_r/U contours, the iso-u/U remain unchanged for $h/c_r = 0.6$ and $h/c_r = 0.4$. In the case of $h/c_r = 0.2$, it can be seen that the spanwise boundary layer rolls up due to the presence of the flat plate, and it is indicated in Figure 4-1(k).

4.2. Streamwise progression of vortex system for baseline swept wing

The development and evolution of TV, SV and GV are shown in the Figure 4-2 at $h/c_r = 0.15$ and $h/c_r = 0.05$. The said ground proximities are chosen since the progression of TV, GV and TV, SV can be seen separately. The dashed arrows marked in red indicate the ζ_{peak} of the TV, light blue indicate ζ_{peak} of GV and green indicate the ζ_{peak} of SV. The positive value for the magnitude of GV indicates it spins in the same direction as TV and the negative sign for the magnitude of SV denotes that SV rotates in the opposite direction.

The formation of GV can be explained in two ways. The first is based on the concept of spanwise ground vortex filament (SGVF), and the second is due to the rolling up of the longitudinal boundary layer. The first concept purely applies to 3-D wings as there is no vortex system for airfoils. Meanwhile, the second concept applies to both 2-D airfoils and 3-D wings as the
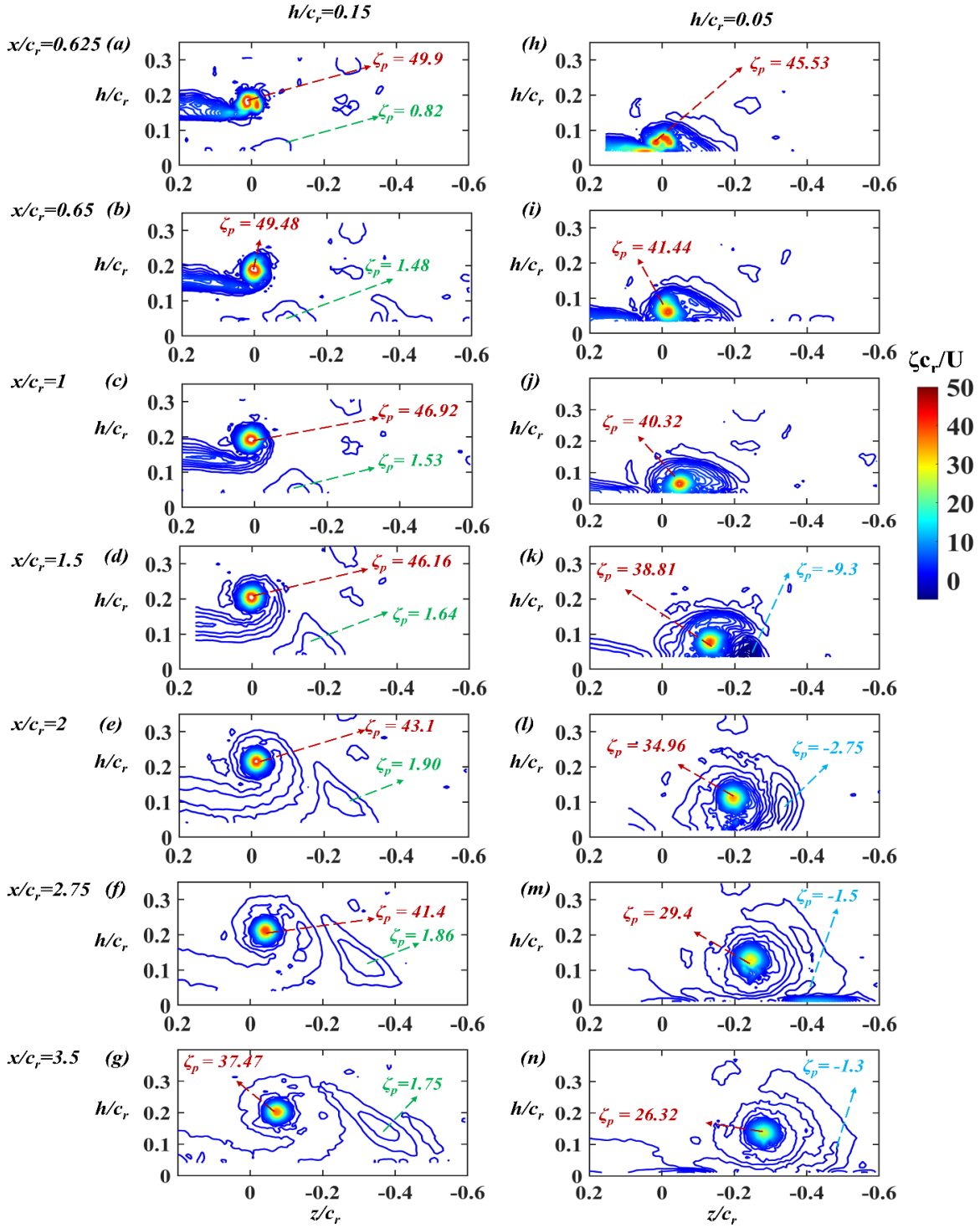
Figure 4-2 Streamwise development of iso-vorticity h/c_r = 0.15 and h/c_r = 0.05 for baseline (The meaning of the coloured lines and arrows is given in the text)

longitudinal boundary layer is present in both cases and is based on the stationary boundary. When the free stream hits the leading edge of the wing, there is a component of the main vortex that

50

travels downwards, and it is called the spanwise ground vortex filament (SGVF) and is responsible for the formation of GV. The GV starts appearing with a small peak value at the wing's trailing edge and builds up in strength as it travels spanwise. This can also be seen as the longitudinal rolling up of the boundary layer. Due to the higher strength of the TV, GV is lifted from the ground. With further progression of TV, it merges with TV, and after a certain spanwise distance, GV seizes to exist. This merging between TV and GV is shown in Figures 4-2 (a) to (g).

Further, at $h/c_r = 0.05$, the wing is in extreme proximity to the ground. Due to this, as TV progresses, a part of the flow rubs against the ground, and after a specific spanwise distance, the boundary layer separates from the ground. After the separation, it rolls up, and a von-Karman vortex sheet is formed. As the flow on either side of the sheet is in the opposite direction, a vortex is generated at the end of the sheet, and it is the counter-rotating SV shown in Figures 4-2 (k) to (n). If ζ_{peak} of the TV for $h/c_r = 0.15$ and $h/c_r = 0.05$ is observed, it can be seen that as the wing moves closer to the ground, there is a decrease in the magnitude of TV, which means that the TV
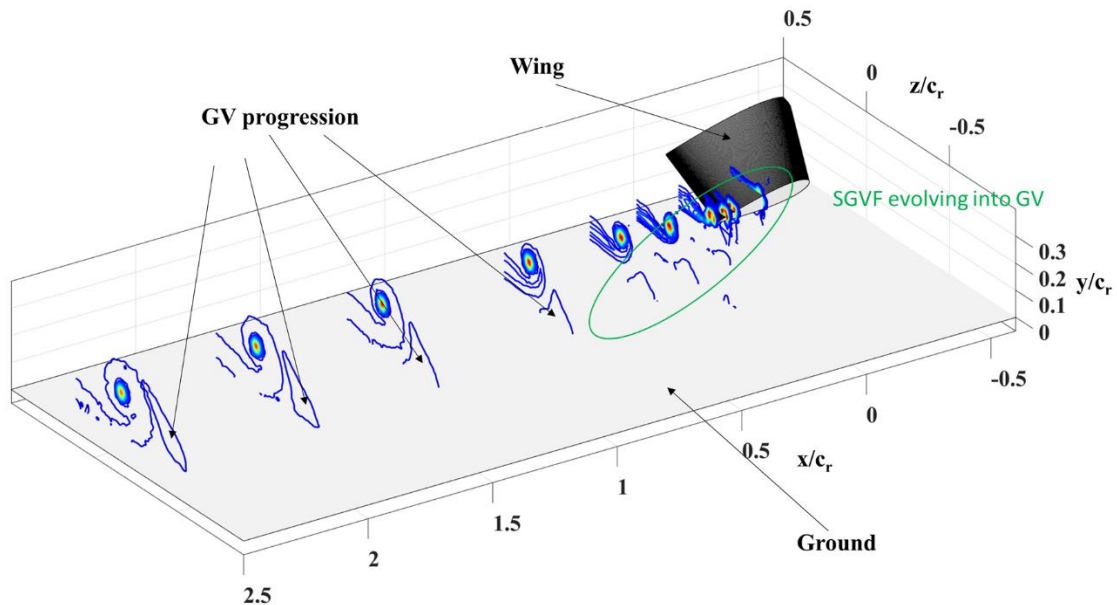
Figure 4-3 Spatial progression of vorticity $h/c_r = 0.15$ for baseline wing

is less intense with decreased ground proximity as part of its strength converted into SV. It can be seen in all the figures from 4-2 (a) to (n), and this decrease in the magnitude of TV is directly responsible for the reduction in C_{Di} and lift increase.

The spatial evolution of the vortex system in 3-D with GV is shown in Figure 4-3. The iso-vorticity contours at $h/c_r = 0.15$ with different spatial locations (x/c_r) are also shown. The ground vortex is formed due to the downward progression of SGVF. It is a conceptual filament that originates at the base of the wing and progresses along the wing's span. Once it reaches the leading edge, it bends with the edge and propagates in the main vortex direction. This SGVF is swept downstream at the trailing edge and gives rise to a co-rotating GV against the fixed ground surface. Ideally, if only GV existed, it should be spiral in nature, but due to its interaction with TV and the surface boundary, the shape of the GV is distorted, and it has an irregular shape, as shown in Figure 4-3. It is important to note that the GV starts right at the wing's trailing edge, proving that it is generated due to SGVF. It is also important to note that if the ground surface were moving instead of the stationary flat plate, there would be no longitudinal boundary layer, and there would be no GV.
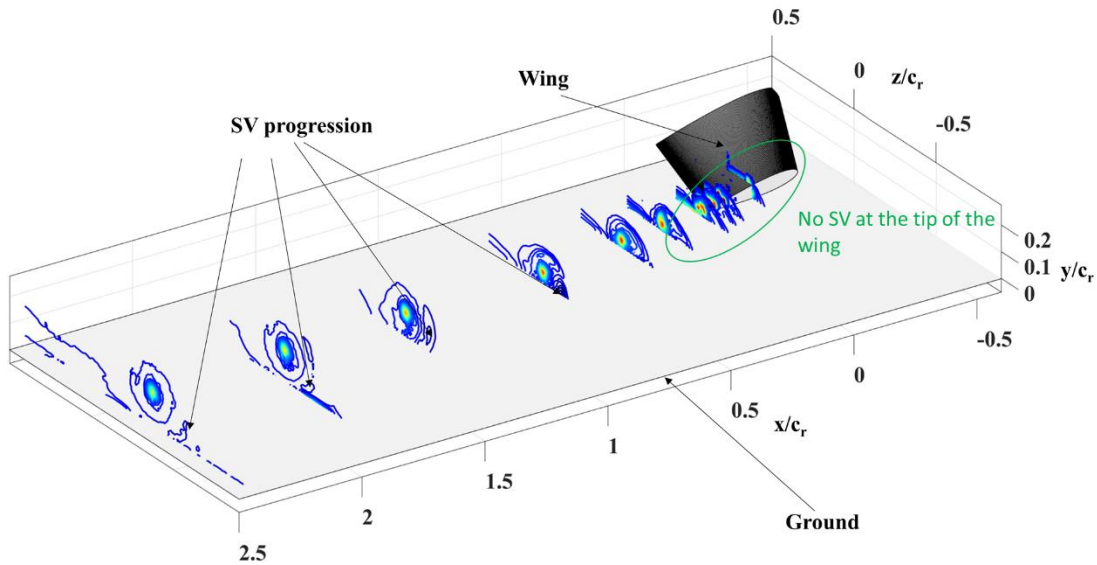

Figure 4-4 Spatial progression of vorticity $h/c_r = 0.05$ for baseline wing

The strength of TV is significantly higher than the strength of GV. Due to which farther downstream, TV lifts GV from the ground, and they merge and propagate as a single vortex system, which is only possible since they rotate in the same direction.

The spatial evolution of the vortex system in 3-D with SV is shown in Figure 4-4. The iso-vorticity contours at $h/c_r = 0.05$ with different spatial locations (x/c_r) are also shown. The generation of SV is purely due to the interaction of TV with the ground. It can be noted that at the trailing edge of the wing, there is no existence of SV. It is only seen as the spanwise boundary layer rolls up, and this only happens after a certain streamwise distance. As the size of the TV increases and the TV progresses, the SV becomes more prominent and more potent as the TV loses its energy to SV.

4.3. Comparison of iso-$\zeta c_r/U$ and iso-u/U contours for baseline wing and wing with 45° and 90° winglets

The vortex system of the baseline wing and the wing with the two winglets differ from each other. Due to the joint between the wing and the winglets, a new vortex comes into existence, and this vortex is called JV. Its ζ_{peak} is denoted by golden dashed arrows and can be seen in Figure 4-5 (b1) to (b5) for the 45° winglet and (c1) to (c5) for the 90° winglet and the red dashed arrows indicate the ζ_{peak} of the TV. The solid green line represents the wing. With the wing moving closer to the ground, it can be seen that there a decremental trend in TV for the wing with no winglet. If a comparison between all three wing arrangements is considered, the TV has the highest magnitude for the wing with no winglet. The wing with the 45° winglet can be considered as a transition between the two cases. For values of $h/c_r > 0.2$, the shape of the vortex is similar to that of the wing with no winglet, and JV does not have substantial values. With further movement of the wing towards the ground, the shape of the vortex system completely changes, and the value of JV is
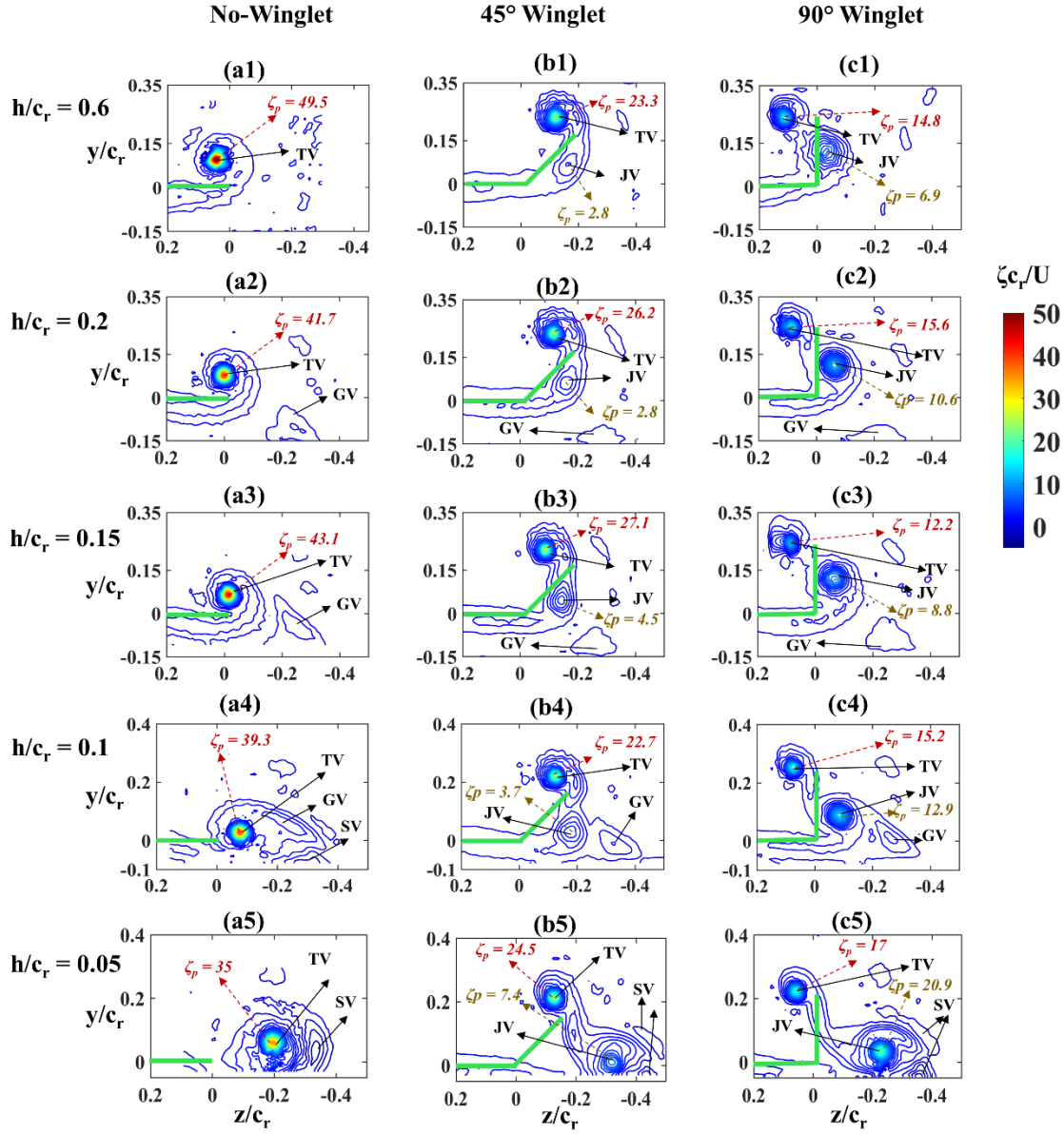
Figure 4-5 Comparison of iso-vorticity contours between (a1) -(a5) baseline wing, (b1) -(b5) wing with 45° winglet and (c1) -(c5) wing with 90° winglet at $x/c_r = 2$ (The meaning of the coloured lines and arrows is given in the text)

significantly higher. It can be noted that the centre of the TV for 45° winglet remains almost the same, but the center of JV moves away from the wing and is entirely outside the span of the wing for $h/c_r = 0.05$ and hence the ζ_{peak} value is large as the JV has plenty of space to rotate freely.
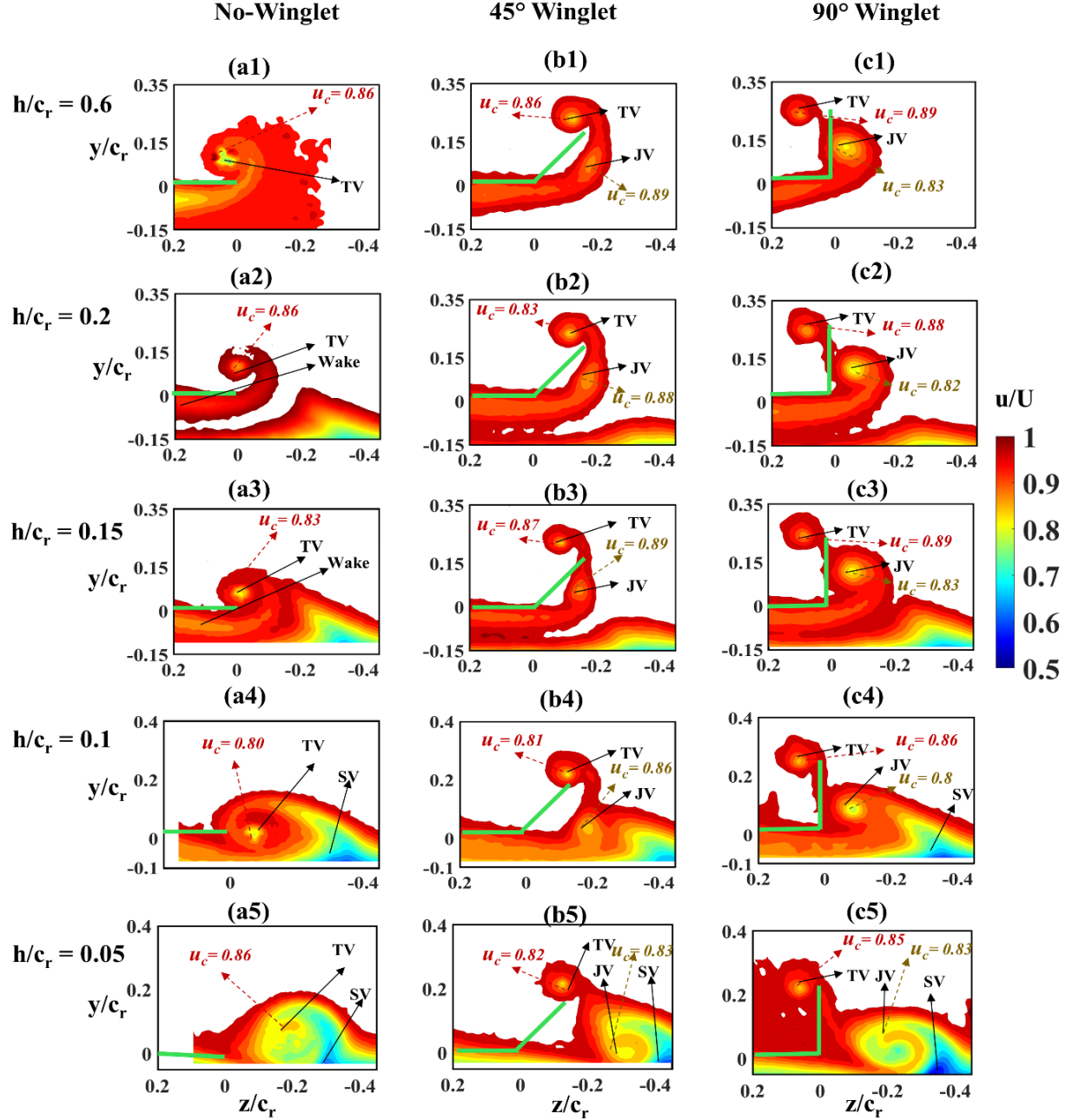
Figure 4-6 Comparison of iso-axial velocity contours between (a1) -(a5) baseline wing, (b1) -(b5) wing with 45° winglet and (c1) -(c5) wing with 90° winglet at $x/c_r = 2$ (The meaning of the coloured lines and arrows is given in the text)

The wing with the 90° winglet is a unique case as the behaviour of the vortex system is distinctive from the other two cases. The TV has comparable values of ζ_{peak} for $h/c_r = 0.6$ to $h/c_r = 0.05$; however, its center seems to stay inside the span. The JV has growing values of ζ_{peak} with closer ground proximity. Figure 4-6 shows the behaviour of axial velocity for the three cases. The red

dashed arrows give the core velocity of TV, and the golden dashed arrows give the core velocity of JV. The boundary layer rolls up at $h/c_r = 0.2$ for the baseline wing, earlier than other winglet arrangements. For the wing with 45° winglet and 90° winglet, the roll up occurs at ground proximity of $h/c_r = 0.15$. Figures 4-5 and 4-6 show that the wing with a 90° winglet has better vorticity control than the other two arrangements.

4.4. Variation of vortex flow properties and parameters with changing ground proximity

The completion of vortex development can be understood from Figure 4-7 (a). It is evident from the figure that $v_{\theta\,max} = |v_{\theta\,min}| = v_{\theta\,peak}$ for all cases for ground proximities, and also, the behaviour is almost axisymmetric for all cases with even different wing attachments. Hence it can be stated that the core vortex is fully developed in all cases at $x/c_r = 2$. Also, r_c can be identified for each case from the figure, and its magnitudes seem to vary with the longitudinal distance between $v_{\theta max}$ and $v_{\theta min}$. As the wings come close to ground proximity, there is a variation in r_c, and this change is because the lifting line is closer to the ground and results in a changing vortex size. As h/c_r further reduces, the appearance of GV and SV also influences the change of r_c. Figure 4-7 (b) shows the variation of u/U for $h/c_r = 0.6$ and $h/c_r = 0.05$, which are two extreme cases, and the u_c
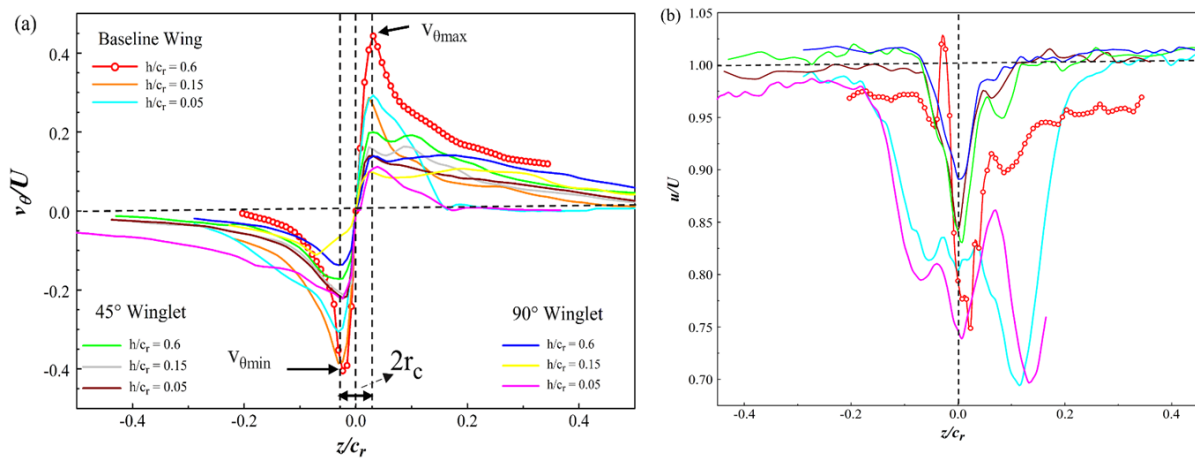
Figure 4-7 (a) Normalized tangential and (b) axial velocity distributions

56

is always wake-like. The reason for the wake-like behaviour of u_c at $h/c_r = 0.6$ is because of the higher wake generated by the wing. The flow structure, even outside the core, is also dominated by the remaining wing wake. At $h/c_r = 0.05$, the u_c is wake-like due to the interaction of boundary
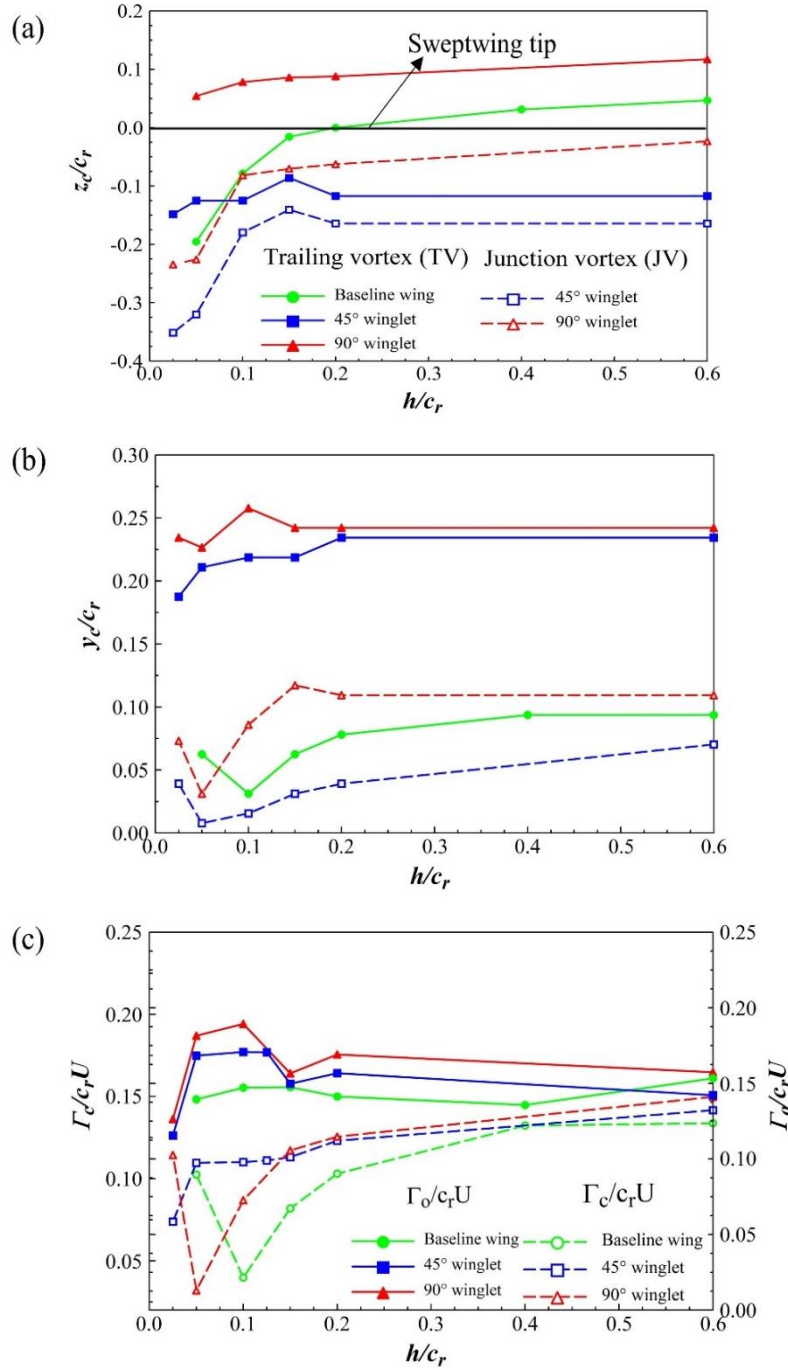

Figure 4-8 Position of vortex centers and circulation at $x/c_r = 2$

layer flow generated by the ground. This wake-like behaviour is because of massive flow separation on the wing's upper surface. Figures 4-8(a) and (b) specify the spanwise position of both TV and JV vortex centres. For the baseline wing, the vortex center of the TV seems to be inside the span of the wing for OGE and moves outside the span as h/c_r decreases. Unlike the baseline wing, the wing with winglets behaves differently. For the 45° winglet, the location is always outside the span for both TV and JV. However, for the 90° winglet, the location of the center of the TV never comes out of the span of the wing, and the location for JV always remains outside the span. Figure 4-8 (b) specifies the longitudinal position of the vortex center. It can be seen that the location of the center of the TV is almost linear in the longitudinal direction, with a decrease in ground proximity for both winglets. It is evident from the figure that the vortex rebounds from the ground for TV of the baseline wing and JV of the wing with winglets as $h/c_r <$ 0.1; this is because of ram pressure and limited space for the vortex to propagate downward further.

A slight increase in the value of total circulation ($\Gamma_o/c_r U$) is seen from the $h/c_r = 0.6$ to 0.1 for wing with winglets, but the baseline wing shows a very wobbly trend for $h/c_r = 0.6$ to $h/c_r = 0.2$, as shown in Figure 4-8 (c). This increase can be attributed to the generation of GV, which adds to the value of TV. However, for values less than $h/c_r < 0.1$, the $\Gamma_o/c_r U$ sharply decreases for all three wing arrangements because, at such extreme proximity, the GV has already merged with TV, and the counter-rotating SV has its decremental effects on $\Gamma_o/c_r U$. The core circulation ($\Gamma_c/c_r U$) shows a decreasing trend for all values of h/c_r in the case of the wing with the 45° winglet. Nevertheless, the values $\Gamma_c/c_r U$ show a steady decrease till $h/c_r = 0.1$ for the baseline wing and $h/c_r = 0.05$ for the wing with the 90° winglet. However, when both these wing arrangements reach very close to the ground, the core strength increases in order to compensate for the lack of space and vorticity strength at the core rises as the vortex is tightly packed.

4.5. Calculation of lift-induced drag (C_{Di})

Maskell's wake integral method is used to calculate the coefficient of lift-induced drag, which is discussed in this section, and it is compared with Maskell's method using the effective aspect ratio (AR_{eff}). The formula for calculation of $C_{Di} = \frac{D_i}{\frac{1}{2}\rho U^2 S}$ and the lift-induced drag D_i is calculated by the below formula,

$$D_i = \frac{\rho_\infty}{2}\left[\iint \psi\,\zeta\,dy\,dz - \iint \phi\,\sigma\,dy\,dz - \iint (1 - M_\infty^2)(\Delta u)^2\,dy\,dz\right] \tag{4.1}$$

Where ζ is obtained from v,w – crossflow measurements, ψ and ϕ are stream function and σ velocity potential respectively, and $\sigma = \frac{\partial v}{\partial y} + \frac{\partial w}{\partial z}$. The procedure followed for deriving the final formula is given in appendix A. The final formula obtained is given below as equation 4.2 (Please refer to Appendix A for the meaning of notations)

$$D_i = \frac{\rho}{2}\sum_{i=2}^{n-1}\sum_{j=2}^{m-1}\left(\psi_{i,j}\,\zeta_{i,j} - \phi_{i,j}\,\sigma_{i,j}\right)\eta^2 \tag{4.2}$$

The value of C_{Di} in ground effect is also estimated using the below formula,

$$C_{Di} = \frac{C_{L,OGE}^2}{\pi\,e\,AR_{eff}} \tag{4.3}$$

Where $C_{L,OGE}$ is the coefficient of lift outside ground effect at $\alpha = 8°$, e is known as Oswald's efficiency factor, which has a value of 1 for the elliptical wing, but for the swept and tapered wing is set to 0.85. AR_{eff} represents effective aspect ratio which is given by $AR_{eff} = b'^2/S$ where b' is the effective span and S is the area of the swept wing. It can be seen from Figure 4-9 that in both cases, the wing with the 90° winglet has less C_{Di} than the wing without winglets. The wingtip
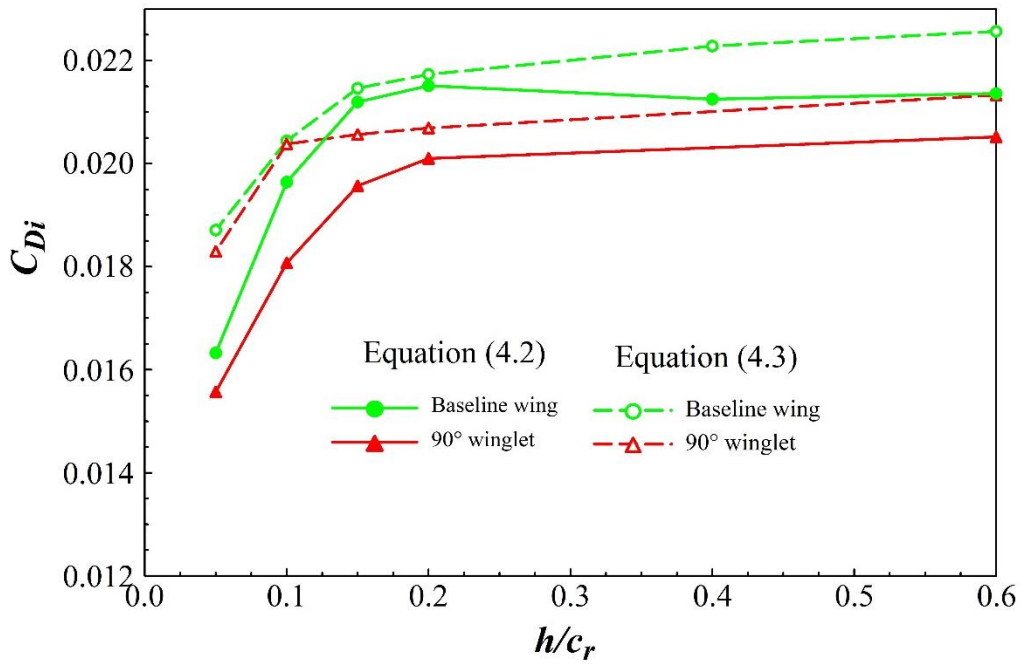
Figure 4-9 Graph of C_{Di} vs h/c_r calculated using two methods

vortices are of the wing with winglets are less intense compared to the baseline wing. Hence the lift-induced drag, in general, is much lesser for wing with winglets. It also can be noted that for the baseline wing, the calculation of C_{Di} reaches a local maximum at $h/c_r = 0.2$ based on equation 4.2, which can be attributed to the appearance of GV. However, this trend is not seen as per equation 4.3. Nevertheless, in the case of equation 4.2 and equation 4.3, the value of C_{Di} reaches a minimum value when the wing approaches the ground. This is because there is a sudden surge in $C_{L,IGE}$. This surge is because at very close proximity, the downwash angle of the wingtip vortices is reduced, and this attributes to an upward reaction and an increase in $C_{L,IGE}$, thereby reducing C_{Di}. The surge in $C_{L,IGE}$ can also be attributed to the outward movement of the wingtip vortices. It is important to note that the values obtained by equation 4.3 merely give lower or upper bound for lift-induced drag coefficient since the equation is based on inviscid theory and may not be considered as accurate as equation 4.2.

4.6. Estimation of C_L in ground effect

The estimation of $C_{L,IGE}$ is started by calculation of circulation using the wake generated behind the swept wing. The circulation of the swept wing is calculated using Stoke's theorem. It is calculated by area integration of vorticity for a given TV, SV and GV. Estimation of C_L for baseline swept wing is pursued by the concept of K-J theorem based on the formula below,

$$C_L = \frac{2\,\Gamma \times b'}{U \times S} \tag{4.4}$$

Where Γ, is the circulation of vortices and b' is the useful span, and $S = \frac{1}{2}\, b \times (c_r + c_t)$ is the area of the swept wing, and U is the free stream velocity. Based on the above theorem, three formulas have been derived to get the circulation of the swept wing in ground effect. The formulas are given below,

$$C_{L1} = \frac{2 \times \{\,\Gamma(TV) - \Gamma(SV) + \Gamma(GV)\,\} \times b'(TV)}{U \times S} \tag{4.5}$$

$$C_{L2} = \frac{2 \times \{\Gamma(TV) + \Gamma(SV) + \Gamma(GV)\} \times b'(TV)}{U \times S} \tag{4.6}$$

$$C_{L3} = \frac{2 \times \{\Gamma(TV) \times b'(TV) + \Gamma(SV) \times b'(SV) + \Gamma(GV) \times b'(GV)\}}{U \times S} \tag{4.7}$$

Equations 4.5 and 4.6 are based on the concept of the effective span of the dominant vortex regardless of the span of other vortices. However, equation 4.7 has a different approach altogether, which is based on the fact that the strength of the vortex and the effective span of that particular vortex both play a vital role in the estimation of lift coefficient. This assumption is valid because the span-dominated ground effect depends heavily on the downwash angle and the effective span.

The circulation of each vortex is given in Table 4; also, the effective span for vortices has been calculated and given in Table 4. These circulation values are calculated by manually dividing the vortex into its components in an excel spreadsheet and then summing up those values to get the circulation. The vortex system of the swept wing without the winglet behaves in the same manner as the rectangular wing. However, when the winglets are introduced, the nature of the variation of vortices changes.

Table 4 Circulation values for the swept wing and effective spans

h/c_r	$\Gamma(TV)$ m^2/s	$\Gamma(SV)$ m^2/s	$\Gamma(GV)$ m^2/s	b'(TV)	b'(SV)	b'(GV)
0.6	0.648944	0	0	1.0019	0	0
0.4	0.649536	0	0	1.0083	0	0
0.2	0.638510	0	0.033001	1.021	0	1.12003
0.15	0.656248	0	0.043264	1.0273	0	1.11369
0.1	0.737059	-0.01975	0	1.0527	1.15176	0
0.05	0.734635	-0.16121	0	1.1003	1.15810	0

Table 5 C_L values using the three formulas for baseline swept wing

h/c_r	C_{L1}	C_{L2}	C_{L3}
0.6	0.65124	0.65124	0.65124
0.4	0.65597	0.65597	0.65597
0.2	0.68671	0.68671	0.68998
0.15	0.71979	0.71979	0.72353
0.1	0.75635	0.79801	0.79996
0.05	0.63198	0.98733	0.99665

The circulation of baseline swept wing is initially calculated, and $C_{L,IGE}$ is estimated with equations 4.5, 4.6 and 4.7. It can be seen from Table 4 that the GV is not present for $h/c_r < 0.1$, and SV starts to appear only below $h/c_r < 0.1$ because the TV should be as close as possible for the TV to rub on the ground. At $h/c_r = 0.05$, the effective span is the largest for SV, and the magnitude of SV reaches 20% of TV, which can be seen in the last row of Table 4. Also, at $h/c_r = 0.05$, the circulation of TV is the same as the circulation at $h/c_r = 0.1$, which only means that the TV loses significant strength to SV at $h/c_r = 0.05$. Table 5 shows the C_{L1}, C_{L2} and C_{L3} for the baseline swept wing.
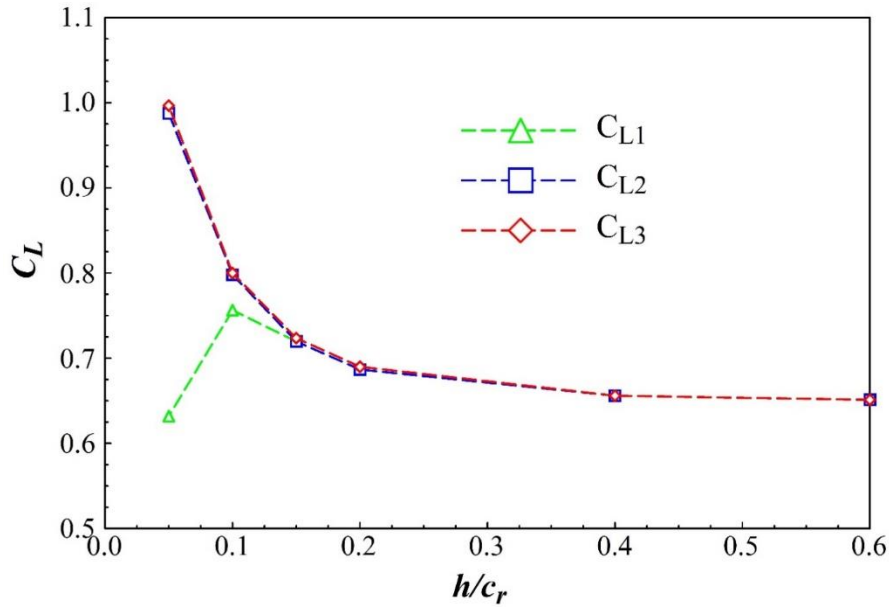
Figure 4-10 Graph of C_L versus ground distance comparing C_{L1}, C_{L2}, C_{L3}

It is noted from Table 5 that C_{L1} is far off when compared to C_{L2} and C_{L3}. This is because the formula involves the negation of the value of SV. When the circulation value is further multiplied by the span, the net product is large, and it has a decremental effect on C_{L1}. It can be seen from the above Figure 4-10 that all three curves are in agreement with each other with slight deviations. For values between $h/c_r = 0.6$ and $h/c_r = 0.15$ all C_L values agree with each other. For values $h/c_r < 0.15$, the deviation is slightly larger. Circulation is large at these values, leading to a slight overshoot of C_{L2} and C_{L3} values. It can be observed that the deviation between C_{L1}, C_{L2}, and C_{L3}

is quite large, which suggests that equation 4.5 may not be an accurate formula as it negates the strength of SV. It is also clear from Figure 4-10 that C_{L1} varies a lot more than C_{L2} and C_{L3}. This variation happens because at such close ground proximity, the circulation of SV is as high as 20% of TV, and SV's value is subtracted from equation 4.1. This significant magnitude, along with a larger effective span of TV, only adds to the decline of C_{L1}.

The next step is to estimate $C_{L,IGE}$ of the swept wing with winglets. As mentioned earlier, due to the introduction of the winglets, there is a new vortex called JV. This JV is of higher importance than TV in the case of the wing with winglets because this JV is the one that is responsible for the reduction in C_{Di} and hence an increase in $C_{L,IGE}$. JV increases the effective span of the wing when winglets are introduced instead of TV. Only the estimation with 90° winglet arrangement is done because, for the 45° winglet, there is difficulty in calculating the strength of the vortices for some ground distance values as the vortices are too closely bound. The three formulas given below are used to estimate C_L for the wing with the 90° winglet.

$$C_{L1}(90°) = \frac{2 \times \{\Gamma(TV) - \Gamma(SV) + \Gamma(GV) + \Gamma(JV)\} \times b'(JV)}{U \times S} \tag{4.8}$$

$$C_{L2}(90°) = \frac{2 \times \{\Gamma(TV) + \Gamma(SV) + \Gamma(GV) + \Gamma(JV)\} \times b'(JV)}{U \times S} \tag{4.9}$$

$$C_{L3}(90°) = \frac{2 \times \{\Gamma(TV) \times b'(TV) + \Gamma(SV) \times b'(SV) + \Gamma(GV) \times b'(GV) + \Gamma(JV) \times b'(JV)\}}{U \times S} \tag{4.10}$$

It can be seen from equations 4.8 and 4.9 that b'(JV) is used as the effective span. With the introduction of the winglet, it can be noted that the TV moves inwards when compared to the baseline wing. Hence, the span of JV compensates for the inward movement of TV by increasing

the effective span of the wing. From Tables 3 and 4, we can see that the circulation of the TV for the baseline wing has reduced in strength. Due to the introduction of the winglet, the strength of the TV of the baseline wing is not divided equally. Hence, both JV and TV for the swept wing with 90° winglet have varying circulation values. Table 6 below shows the circulation and effective span of the swept wing with the 90° winglet.

Table 6 Circulation values for the swept wing with the 90° winglet and effective spans

h/c_r	Γ(TV) m²/s	Γ(JV) m²/s	Γ(SV) m²/s	Γ(GV) m²/s	b'(TV)	b'(JV)	b'(SV)	b'(GV)
0.6	0.2559	0.4049	0	0	0.9684	1.0255	0	0
0.2	0.2733	0.3885	0	0.0705	0.9803	1.0414	0	1.0947
0.15	0.2351	0.4594	0	0.0616	0.9811	1.0446	0	1.1231
0.1	0.2680	0.4100	0	0.1215	0.9842	1.0492	0	1.1175
0.05	0.2678	0.6086	-0.0749	0	0.9940	1.1078	1.1598	0

Table 7 C_L values using the three formulas for swept wing with the 90° winglet.

h/c_r	C_{L1} (90°)	C_{L2} (90°)	C_{L3} (90°)
0.6	0.678763	0.678763	0.6641109
0.2	0.763916	0.763916	0.7509436
0.15	0.790962	0.790962	0.7808533
0.1	0.840259	0.840259	0.8311105
0.05	0.889294	1.055571	1.028949
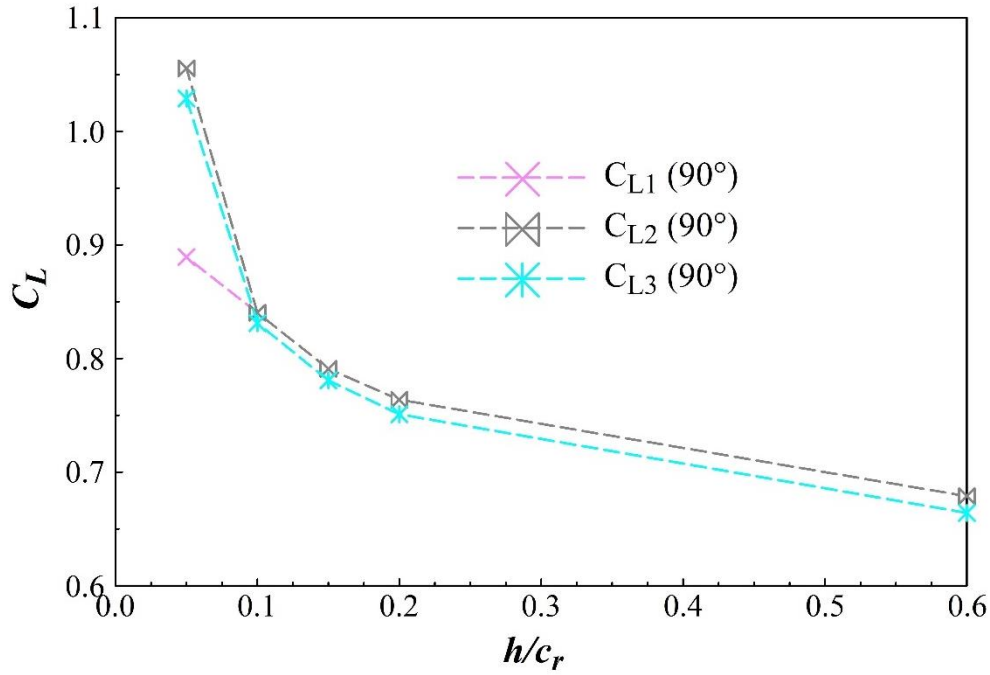
Figure 4-11 Graph of C_L versus ground distance comparing C_{L1} (90°), C_{L2} (90°) and C_{L3} (90°)

Table 7 shows the values of C_{L1} (90°), C_{L2} (90°) and C_{L3} (90°) that are obtained from the formulas for the swept wing with winglet. Figure 4-11 shows the plot of coefficient of lift versus ground distance and a comparison between C_{L1} (90°), C_{L2} (90°) and C_{L3} (90°). Figure 4-11 shows that the values of C_{L1} (90°) and C_{L2} (90°) are the same till $h/c_r = 0.1$. For ground proximity below $h/c_r = 0.1$ SV start appearing, and as in the previous case, there is a decrement in the value of C_{L1} (90°) due to negation of SV. It should be noted that there is a clear gap between C_{L3} (90°) and C_{L2} (90°); this is because of the use of the effective span of JV in estimation C_{L2} (90°), due to which the coefficient of lift of the value is amplified. However, since C_{L3} (90°) formula, the respective effective spans are used, this formula can be termed as more accurate than the others.

Two vital observations have been made during the theoretical calculation of C_L, and they are given as follows (a) For the rectangular semi-wing, the most crucial point in the accuracy of the C_L is the estimation of circulation. Bombardier's estimation of circulation is $\Gamma_o/cU = 0.262$, the

66

estimation by force balance is $\Gamma_o/cU = 0.331$ (Lu and Lee (2019)), and the current value of $\Gamma_o = 0.7565$ m^2/s obtained form $C_{L,OGE}$, which leads to a $\Gamma_o/cU = 0.18011$. Now for all the above cases, the decremental factor of the effective span is ignored. None of the values match each other. The conclusion from this point is that circulation accuracy may be in question and needs to be evaluated. This discrepancy might also propagate in the estimation of circulation of the swept wing as the same wind tunnel, and the same instrumentation is used in this experiment. (b) The $C_{L,OGE}$ value of the swept wing obtained for the same wing is 0.73 (Gerentoks and Lee (2006b)). The swept-back semi-wing has a NACA 0015 profile, and its $C_{L,OGE}$ is compared with $C_{L,OGE}$ of the NACA 0012 rectangular semi-wing, which is equal to 0.5678 (Lu and Lee (2019)) at a comparable freestream and α. Also, the $C_{L,OGE}$ from the current estimation is 0.6641. The $C_{L,OGE}$ of swept semi-wing is higher than the semi-rectangular wing. It is because the AR of the rectangular wing in question is much lower than the swept wing.
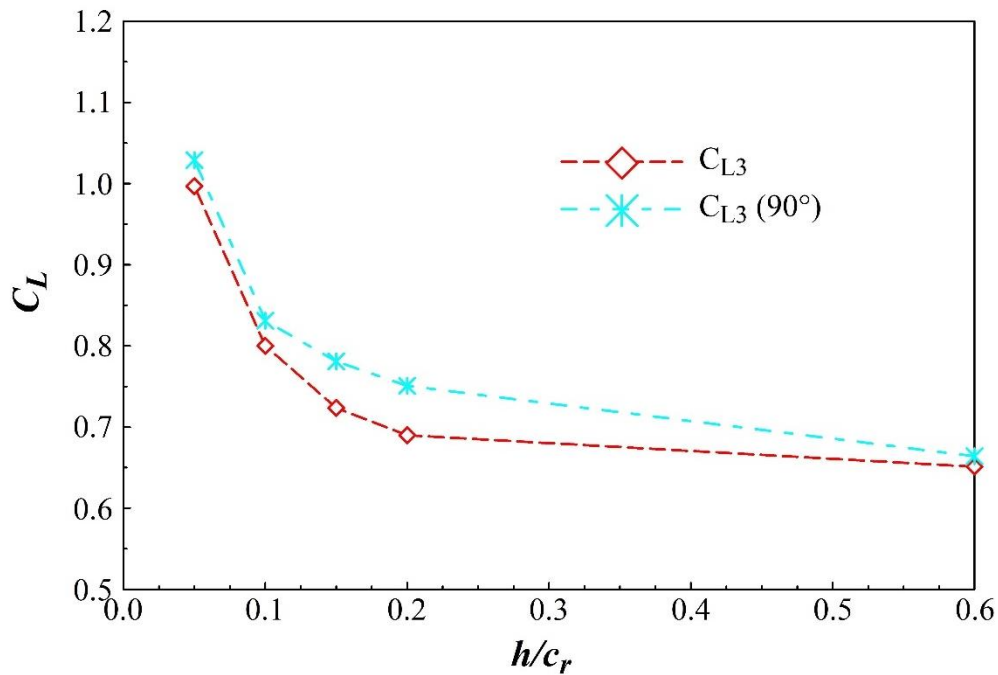
Figure 4-12 Graph of C_L vs ground distance comparing C_{L3} of the sweptwing and C_{L3} (90°) sweptwing with winglets.

Based on the above information and the other graphs above, it can be concluded that the C_{L3} and C_{L3} (90°) are comparatively more accurate than the other formulae. Figure 4-12 shows the comparison of the final estimation curves. It is evident from the figure that the wing with 90° winglet has a better performance than a wing without winglets.

5. Conclusion

5.1. Changes in vortex structure and aerodynamic coefficients

The research project's objective was to understand the impact of ground proximity on the wingtip vortex generated by the swept wing with the NACA 0015 profile. The objective was also to understand the impact of implementation on winglets on the wingtip vortices generated by winglet attachments that could reduce drag in new ground effect vehicles, and both these above objectives have been completed. Estimations of C_L and C_{Di} concluded significant variations in C_L and C_{Di} with changing ground distances. An increase in C_L was seen due to the span-dominated ground effect at close ground proximity, there was minimal space for the vortex to move, and hence the ram pressure created a significant increase in lift. Due to the above reason, there was also a significant decrease in C_{Di}. The average decrease in C_{Di} based on equation 4.2 is 5 %, and the average decrease in C_{Di} based on equation 4.3 is 6 %. The maximum decrease in C_{Di} at 5% ground proximity compared to OGE is 20% from equation 4.2 and 30% from equation 4.3.

The estimation of C_L for swept wing with winglet showed an additional JV that was present, which shared some of the strength of TV and hence had a higher C_L than the baseline wing. It was also seen that the wing with 90° winglet was a much better combination to have than just the baseline wing and had a positive impact both on C_L and C_{Di}. The average increase in lift due to the 90° winglet was 5.17%, which was calculated based on the C_{L3} and C_{L3} (90°). Thus, a 53% increase in $C_{L,IGE}$ at 5% ground distance is obtained compared to $C_{L,OGE}$ for baseline wing and wing with winglet.

A change in vortex strength and shape was observed due to changing ground distance and change in position of the vortex center. The vortex center moved both in the longitudinal direction and

spanwise direction. As the vortex progressed, it was also observed that the vortex hit the ground and bumped back up due to a lack of space for its propagation.

5.2. Future work

The future work for the swept wing and swept wing with winglets would be to validate the prediction of C_L using a force balance experiment. The C_L has been estimated only for one 90° winglet. It would be interesting to see the performance of the swept wing for various negative winglet dihedrals. The study must also be extended to the effect of ground proximity on vortices generated by various shapes of wing attachments that have been discussed in the literature for OGE. The current experimental work was carried out in fixed ground conditions or also called a no-slip boundary condition. It would be interesting to see the performance of the swept wing in moving ground. This condition exactly replicates the performance of the wing in real-world cases.

References

Ahmed, M. R., and Sharma, S. D. (2005). An investigation on the aerodynamics of a symmetrical airfoil in ground effect. *Experimental Thermal and Fluid Science*, *29*(6), 633–647.

Ahmed, M. R., Takasaki, T., and Kohama, Y. (2007). Aerodynamics of a NACA4412 airfoil in ground effect. *AIAA Journal*, *45*(1), 37–47.

Altaf, A., Omar, A. A., Asrar, W., and Jamaluddin, H. B. L. (2011). Study of the reverse delta wing. *Journal of Aircraft*, *48*(1), 277–286.

Barber, T. (2006). Aerodynamic ground effect: A case study of the integration of CFD and experiments. *International Journal of Vehicle Design*, *40*(4), 299-316.

Barber, T. J., Leonardi, E., and Archer, R. D. (2002). Causes for discrepancies in ground effect analyses. *The Aeronautical Journal*, *106*(1066), 653–668.

Barlow, J. B., Rae, W. H., Pope, A., and Pope, A. (1999). *Low-speed wind tunnel testing* (3rd ed.). New York: Wiley.

Brune, G. W. (1994). Quantitative low-speed wake surveys. *Journal of Aircraft*, *31*(2), 249–255.

Carter, A. (1961). Effect of ground proximity on the aerodynamic characteristics of aspect ratio-1 airfoils with and without end plates. *NASA Special Publication,* Report No. NASA TN D-970.

Chow, J. S., Zilliac, G. G., and Bradshaw, P. (1997). Mean and turbulence measurements in the near field of a wingtip vortex. *AIAA Journal*, *35*(10), 1561–1567.

Deshpande, P., Vikraman, A., Anand, S., Antony, R., Dodamani, R., C. S., S., and Ajith Kumar, R. (2021). Experimental investigation of the effect of winglets on the aerodynamic performance of a mini UAV. *Journal of Aerospace Engineering*, *34*(1), 04020089.

Galoul, V. and Barber, T. J. (2007). A Study of an Inverted Wing with Endplates in Ground Effect. *16th Australasian Fluid Mechanics Conference (AFMC)*, Gold Coast, Queensland, Australia

Gerontakos, P., and Lee, T. (2006a). Near-field tip vortex behind a swept wing model. *Experiments in Fluids*, *40*(1), 141–155.

Gerontakos, P., and Lee, T. (2006b). Effect of winglet dihedral on a tip vortex. *Journal of Aircraft*, *43*(1), 117–124.

Han, C., and Cho, J. (2005). Unsteady trailing vortex evolution behind a wing in ground effect. *Journal of Aircraft*, *42*(2), 429–434.

Harvey, J. K., and Perry, F. J. (1971). Flowfield produced by trailing vortices in the vicinity of the ground. *AIAA Journal*, *9*(8), 1659–1660.

Hsiun, C.-M., and Chen, C.-K. (1996). Aerodynamic characteristics of a two-dimensional airfoil with ground effect. *Journal of Aircraft*, *33*(2), 386–392.

Jamei, S., Maimun, A., Mansor, S., Azwadi, N., and Priyanto, A. (2016). Design parametric study of a compound wing-in-ground effect. I: Aerodynamics performance. *Journal of Aerospace Engineering*, *29*(1), 04015022.

Jamei, S., Maimun, A., Mansor, S., Azwadi, N., and Priyanto, A. (2016). Design parametric study of a compound wing-in-ground effect. II: Aerodynamics coefficients. *Journal of Aerospace Engineering*, *29*(1), 04015023.

Jia, Q., Yang, W., and Yang, Z. (2016). Numerical study on aerodynamics of banked wing in ground effect. *International Journal of Naval Architecture and Ocean Engineering*, *8*(2), 209–217.

Kliment, L. K., & Rokhsaz, K. (2008). Experimental investigation of pairs of vortex filaments in ground effect. *Journal of Aircraft*, *45*(2), 622–629.

Ko, L. S. (2017). An experimental investigation of the aerodynamics and vortex flowfield of a reverse delta wing. *Ph.D. dissertation, McGill University,* Montreal.

Ko, L. S., Tremblay-Dionne, V., and Lee, T. (2020). Impact of ground proximity on an inverted delta wing. *Journal of Aerospace Engineering*, *33*(5), 04020047.

Kusunose, K. (1997). Development of a universal wake survey data analysis code. *15th Applied Aerodynamics Conference*: *American Institute of Aeronautics and Astronautics*, Atlanta, GA, U.S.A.

Lee, J., Han, C.-S., and Bae, C.-H. (2010). Influence of wing configurations on aerodynamic characteristics of wings in ground effect. *Journal of Aircraft*, *47*(3), 1030–1040.

Lee, S., and Lee, J. (2014). Aerodynamic characteristics of a rectangular wing in ground proximity. *Journal of Aircraft*, *51*(2), 688–693.

Lee, T., and Choi, S. (2015). Wingtip vortex control via tip-mounted half-delta wings of different geometric configurations. *Journal of Fluids Engineering*, *137*(12), 121105.

Lee, T., and He, S. M. (2018). The trailing vortices generated by a reverse delta wing with different wing configurations. *Aerospace Science and Technology*, *82–83*, 378–393.

Lee, T., and Ko, L. S. (2018). Ground effect on the vortex flow and aerodynamics of a slender delta wing. *Journal of Fluids Engineering*, *140*(7), 071104.

Lee, T., and Pereira, J. (2013). Modification of static-wing tip vortex via a slender half-delta wing. *Journal of Fluids and Structures*, *43*, 1–14.

Lee, T., Majeed, A., Siddiqui, B., and Tremblay-Dionne, V. (2018). Impact of ground proximity on the aerodynamic properties of an unsteady airfoil. *Proceedings of the Institution of Mechanical Engineers, Part G: Journal of Aerospace Engineering*, *232*(10), 1814–1830.

Lee, T., Tremblay-Dionne, V., and Ko, L. (2019). Ground effect on a slender reverse delta wing with anhedral. *Proceedings of the Institution of Mechanical Engineers, Part G: Journal of Aerospace Engineering*, *233*(4), 1516–1525.

Lu, A. (2019). Investigation of the ground effect on wingtip vortex generated by a rectangular NACA0012 Wing. *Master's thesis, McGill University,* Montreal.

Lu, A., and Lee, T. (2020). Passive wingtip vortex control by using tip-mounted half delta wings in ground effect. *Journal of Fluids Engineering*, *142*(2), 021201.

Lu, A., and Lee, T. (2021). Effect of ground boundary condition on near-field wingtip vortex flow and lift-induced drag. *Journal of Fluids Engineering*, *143*(3), 031301.

Lu, A., Tremblay-Dionne, V., and Lee, T. (2019). Experimental study of aerodynamics and wingtip vortex of a rectangular wing in flat ground effect. *Journal of Fluids Engineering*, *141*(11), 111108.

Luo, S. C., and Chen, Y. S. (2012). Ground effect on flow past a wing with a NACA0015 cross-section. *Experimental Thermal and Fluid Science*, *40*, 18–28.

Mantle, P. J. (2016). Induced drag of wings in ground effect. *The Aeronautical Journal*, *120*(1234), 1867–1890.

Maskell, E. C. (1972). Progress towards a method for the measurement of the components of the drag of a wing of finite span. *RAE Technical Report No. 72232*

Moffat, R. J. (1982). Contributions to the theory of single-sample uncertainty analysis. *Journal of Fluids Engineering*, *104*(2), 250–258.

Moore, N., Wilson, P. A., and Peters, A. J. (2002). An investigation into wing in ground effect aerofoil geometry. *RTO-MP-095*, 11–20.

Musaj, M., and Prince, S. (2008). Numerical and experimental investigation of the aerodynamics of an unconventional W-leading edge reversed delta wing in ground effect. *26th international congress of the aeronautical science (ICAS)*, Alaska, USA.

Narayan, G., and John, B. (2016). Effect of winglets induced tip vortex structure on the performance of subsonic wings. *Aerospace Science and Technology*, *58*, 328–340.

Orloff, K. L. (1974). Trailing vortex wind-tunnel diagnostics with a laser velocimeter. *Journal of Aircraft*, *11*(8), 477–482.

Puel, F., and de Saint Victor, X. (2000). Interaction of wake vortices with the ground. *Aerospace Science and Technology*, *4*(4), 239–247.

Qin, Y., Liu, P., Qu, Q., Zheng, Y., and Agarwal, R. K. (2018). Numerical study of the aerodynamic forces and flow physics of a delta wing in mutational ground effect. *2018 Applied Aerodynamics Conference*. Presented at the 2018 Applied Aerodynamics Conference, Atlanta, Georgia: American Institute of Aeronautics and Astronautics.

Qu, Q., and Agarwal, R. K. (2017). Chord-dominated ground-effect aerodynamics of fixed-wing UAVs., *Advanced UAV Aerodynamics, Flight Stability and Control* (pp. 201–254). Chichester, UK: John Wiley & Sons, Ltd.

Qu, Q., Lu, Z., Guo, H., Liu, P., and Agarwal, R. K. (2015). Numerical investigation of the aerodynamics of a delta wing in ground effect. *Journal of Aircraft*, *52*(1), 329–340.

Qu, Q., Wang, W., Liu, P., and Agarwal, R. K. (2015). Airfoil aerodynamics in ground effect for wide range of angles of attack. *AIAA Journal*, *53*(4), 1048–1061.

Ramaprian, B. R., and Zheng, Y. (1997). Measurements in rollup region of the tip vortex from a rectangular wing. *AIAA Journal*, *35*(12), 1837–1843

Raymer, D. P. (2018). *Aircraft design: A conceptual approach*. AIAA education series. Reston, VA: American Institute of Aeronautics and Astronautics, Inc.

Rozhdestvensky, K. V. (2006). Wing-in-ground effect vehicles. *Progress in Aerospace Sciences*, *42*(3), 211–283.

Sohn, M. H., and Chang, J. W. (2012). Visualization and PIV study of wing-tip vortices for three different tip configurations. *Aerospace Science and Technology*, *16*(1), 40–46.

Spalart, P. R. (1998). Airplane trailing vortices. *Annual Review of Fluid Mechanics*, *30*(1), 107–138.

Steinbach, D. (1997). Comment on "aerodynamic characteristics of a two-dimensional airfoil with ground effect." *Journal of Aircraft*, *34*(3), 455–456.

Steinbach, D., and Jacob, K. (1991). Some aerodynamic aspects of wings near ground. *Transactions of the Japan Society for Aeronautical and Space Sciences*, *34*(104), 56–70.

Suh, Y. B., and Ostowari, C. (1988). Drag reduction factor due to ground effect. *Journal of Aircraft*, *25*(11), 1071–1072.

Tremblay-Dionne, V. (2017). An experimental investigation of aerodynamic properties and flowfield of a NACA 0015 airfoil in ground effect. *Master's thesis, McGill University,* Montreal.

Tremblay-Dionne, V., and Lee, T. (2018). Ground effect on the aerodynamics of a naca 0015 airfoil with a plain trailing-edge flap. *Fluid Mechanics research International Journal*, *2*(1) 6-11.

Tremblay-Dionne, V., and Lee, T. (2021). Discrepancy in the aerodynamic property and flowfield of a symmetric airfoil produced by the stationary and moving ground effect. *Journal of Fluids Engineering*, *143*(2), 021301.

Turner, T. R. (1966). Endless-belt technique for ground simulation. *NASA Special Publication*, *116*, 435.

Wang, H., Teo, C. J., Khoo, B. C., and Goh, C. J. (2013). Computational aerodynamics and flight stability of wing-in-ground (Wig) craft. *Procedia Engineering*, *67*, 15–24.

Wang, Y., Liu, P., Hu, T., and Qu, Q. (2016). Investigation of co-rotating vortex merger in ground proximity. *Aerospace Science and Technology*, *53*, 116–127.

Yang, W., Yang, Z., and Ying, C. (2010). Effects of design parameters on longitudinal static stability for WIG craft. *International Journal of Aerodynamics*, *1*(1), 97-113.

Yeung, A. R. K., and Lee, B. H. K. (1999). Particle image velocimetry study of wing-tip vortices. *Journal of Aircraft*, *36*(2), 482–484.

Yun, L., Bliault, A., and Doo, J. (2010). *WIG craft and ekranoplan: Ground effect craft technology*. Springer US.

Zerihan, J., and Zhang, X. (2000). Aerodynamics of a single element wing in ground effect. *Journal of Aircraft*, *37*(6), 1058–1064.

Zhang, X., and Zerihan, J. (2003). Aerodynamics of a double-element wing in ground effect. *AIAA Journal*, *41*(6), 1007–1016.

Zhang, X., and Zerihan, J. (2004). Edge vortices of a double element wing in ground effect. *Journal of Aircraft*, *41*(5), 1127–1137.

Zhou, J., Sun, C., and Daichin. (2020). Drag reduction and flow structures of wing tip sails in ground effect. *Journal of Hydrodynamics*, *32*(1), 93–106.

Appendix A: Derivation of Formula for C_{Di}

The momentum balance approach is used to calculate drag due to lifting surfaces, and the following conditions are assumed:

- Incompressible and steady-state flow

- Solid walls

- Inlet and outlet of control volume are assumed to have a constant surface area.

- Shear stress is neglected since Re is low.

Using the mass conservation principle, we get:

$$0 = \rho V_2 A_2 = \rho_1 V_1 A_1 \tag{A1.1}$$

$$V_2 A_2 = V_1 A_1 \tag{A1.2}$$

Where V_1 is the total velocity, and A_1 is the cross-sectional area at control surface 1. V_2 is the total velocity, and A_2 is the cross-sectional area at control surface 2. Hence, we can write the law of conservation of momentum as

$$D = \iint_{CS} (P_\infty - P) + \rho \, (u_\infty^2 - u^2) \, dS \tag{A1.3}$$

Where P and u are the static pressure and velocity of the freestream, however, it can be noted that static pressure can be expressed in terms of total pressure as,

$$p_\infty = P_\infty + \frac{1}{2} \, \rho u_\infty^2 \tag{A1.4}$$

Then equation A1.3 reduces to

$$D= \iint_{CS} \left[[p_1 - p_2] + \frac{1}{2}\rho \ (v^2 + w^2) + \frac{1}{2}\rho \ (u_\infty^2 - u^2) \right] dS \qquad \text{(A1.5)}$$

Equation A1.5 has three terms, first is the pressure drag, second is the vortex drag, and the last one is the profile and induced drag. However, to calculate the total drag, the term in the integral must be integrated over the entire wake.

When total wake is taken, the calculation of drag becomes inaccurate; hence, the measurement area should be based on the viscous wake. An artificial velocity is used to describe the viscous wake velocity profile. The artificial velocity correlates the axial velocity with the local pressure profile,

$$u^{*2} = u^2 + \frac{2}{\rho}(p_1 - p_2) \qquad \text{(A1.6)}$$

Where u is the artificial velocity. A new velocity called perturbation velocity ($u' = u^* - u_\infty$) was also introduced, using perturbation velocities into equation (A1.5), the drag simplifies to:

$$D = \iint_{CS} (p_1 - p_2)dS + \frac{1}{2}\rho \iint_{CS} (u^* - u)(u^* + u - 2u_\infty)dS + \frac{1}{2}\rho \iint_{CS} (v^2 + w^2 - u'^2)dS \qquad \text{(A1.7)}$$

Equation (A1.7) can be rearranged into the profile and induced drag components.

$$D_P = \iint_{CS} (p_1 - p_2)dS + \frac{1}{2}\rho \iint_{CS} (u^* - u)(u^* + u - 2u_\infty)dS + \frac{1}{2}\rho \iint_{CS} (v^2 + w^2 - u'^2)dS \qquad \text{(A1.8)}$$

Since in this experiment it is evident that the tunnel wall is far away, the boundary of the tunnel wall does not affect the boundary layer of the wing in the test section, and it can be assumed that u' has almost negligible value and can be eliminated. Hence the equation of drag simplifies to:

$$D_i = \frac{\rho}{2} \iint\limits_{CS} (v^2 + w^2)\, dS \tag{A1.9}$$

It should be noted that the value of the above equation is relatively tiny. However, its value still exists outside of the vortical wake region. Considering stream function ψ, and velocity potential ϕ, the velocity components v and w can be expressed as given below,

$$v = \frac{\partial \phi}{\partial y} + \frac{\partial \psi}{\partial z} \tag{A1.10}$$

$$w = \frac{\partial \phi}{\partial z} - \frac{\partial \psi}{\partial y} \tag{A1.11}$$

Resulting in equation A1.12 from equation A1.11

$$D_i = \frac{1}{2} \rho \iint\limits_{CS} \left[\left(\frac{\partial \phi}{\partial y} + \frac{\partial \psi}{\partial z} \right)^2 + \left(\frac{\partial \phi}{\partial z} - \frac{\partial \psi}{\partial y} \right)^2 \right] dS \tag{A1.12}$$

By using Green's and Divergence theorem, the equation A1.12 can be further simplified to:

$$D_i = \frac{\rho}{2} \iint\limits_{wake} (\psi \zeta - \phi \sigma)\, dS \tag{A1.13}$$

Where ζ is the vorticity and σ is the source term. Boundary treatment is imposed based on boundary conditions:

- Tunnel walls are streamlines, $\psi(\text{wall}) = 0$

- No flow through the walls, $\frac{\partial \phi}{\partial n} = 0$

Hence the calculation of D_i depends on knowing the values of ψ, ζ, ϕ and σ at each point (i, j) in the vortical wake. The central-difference formula calculates the values of vorticity and source terms:

$$\zeta_{i,j} = \frac{\Delta w}{\Delta y} - \frac{\Delta v}{\Delta z} = \frac{w_{i-1,j} - w_{i+1,j}}{2\eta} - \frac{v_{i,j+1} - v_{i,j-1}}{2\eta} \qquad (A1.14)$$

$$\sigma_{i,j} = \frac{\Delta v}{\Delta y} + \frac{\Delta w}{\Delta z} = \frac{v_{i-1,j} - v_{i+1,j}}{2\eta} - \frac{w_{i,j+1} - w_{i,j-1}}{2\eta} \qquad (A1.15)$$

Where $\eta = \Delta y = \Delta z$, i=2,3, ... n-1, j=2,3, ... m-1

The central differencing formula was used for the stream function and velocity potential, and the formula is given below:

$$\zeta_{i,j} = -\nabla^2 \psi_{i,j} \approx -\frac{1}{\eta^2} \left(\psi_{i+1,j} + \psi_{i-1,j} - 4\psi_{i,j} + \psi_{i,j+1} + \psi_{i,j-1} \right) \qquad (A1.16)$$

$$\sigma_{i,j} = -\nabla^2 \phi_{i,j} \approx -\frac{1}{\eta^2} \left(\phi_{i+1,j} + \phi_{i-1,j} - 4\phi_{i,j} + \phi_{i,j+1} + \phi_{i,j-1} \right) \qquad (A1.17)$$

The boundary treatment for the tunnel wall was done in a particular manner. Therefore, the conditions for the left wall, right wall, ceiling, and floor are given below in the same order:

$$\zeta_{i,2} \approx -\frac{1}{\eta^2} \left(\psi_{i+1,2} + \psi_{i-1,2} - 4\psi_{i,2} + \psi_{i,3} \right) \qquad (A1.18)$$

$$\sigma_{i,2} \approx \frac{1}{\eta^2} \left(\phi_{i+1,2} + \phi_{i-1,2} - 3\phi_{i,2} + \phi_{i,3} \right) \qquad (A1.19)$$

$$\zeta_{i,m-1} \approx -\frac{1}{\eta^2} \left(\psi_{i+1,m-1} + \psi_{i-1,m-1} - 4\psi_{i,m-1} + \psi_{i,m-2} \right) \qquad (A1.20)$$

$$\sigma_{i,m-1} \approx \frac{1}{\eta^2} \left(\phi_{i+1,m-1} + \phi_{i-i,m-1} - 3\phi_{i,m-1} + \phi_{i,m-2} \right) \qquad (A1.21)$$

$$\zeta_{n-1,j} \approx -\frac{1}{\eta^2} \left(\psi_{n-2,j} - 4\psi_{n-1,j} + \psi_{n-1,j+1} + \psi_{n-1,j-1} \right) \qquad (A1.22)$$

$$\sigma_{i,2} \approx \frac{1}{\eta^2}\left(\phi_{n-2,j} - 3\phi_{n-1,j} + \phi_{n-1,j+1} + \phi_{n-1,j-1}\right) \tag{A1.23}$$

$$\zeta_{i,2} \approx -\frac{1}{\eta^2}\left(\psi_{3,j} - 4\psi_{2,j} + \psi_{2,j+1} + \psi_{2,j-1}\right) \tag{A1.34}$$

$$\sigma_{i,2} \approx \frac{1}{\eta^2}\left(\phi_{3,j} - 3\phi_{2,j} + \phi_{2,j+1} + \phi_{2,j-1}\right) \tag{A1.35}$$

These equations formed a system of (n-2) × (m-2) equations and (n-2) × (m-2) unknows and these equations can be expressed as $A\vec{X}=\vec{B}$. Where A is the coefficient matrix and $\vec{X}$ is the unknown vector of ψ or ϕ and $\vec{B}$ is the known vector of σ or ζ. To get the value of $\vec{X}$, we need to need to find the product of the matrices BA^{-1}. Since the resolution is quite large, matrix A will grow and be inverted only with a supercomputer. Matrix A was a sparse matrix and would not be larger than Penta diagonal matrix. To reduce the computation time the matrix A was packed into an (n − 2) × (m − 2) by five arrays containing the indices of the non-zero elements. Further computation time was reduced by an iterative successive over-relaxation (SOR) method dependent on the Gauss-Seidel method. It must be noted that the Gauss-Seidel method requires an initial guess value, and to reduce the number of iterations, the initial guess was calculated at a coarse resolution of 25.4 mm, and matrix A had an order of 1632 × 1632. This lower order matrix can be inverted much faster than the original matrix. A relaxation parameter was used to increase the rate of convergence of a matrix, and it was given by,

$$w = \frac{4}{\sqrt{2 + \left[4 - \cos\left(\frac{\pi}{m}\right) + \cos\left(\frac{\pi}{n}\right)\right]^2}} \tag{A1.36}$$

The values of $\vec{X}$ can be determined from the following equation:

$$x_i = (1-w)XO_i + \frac{w\left(-\displaystyle\sum_{j=1}^{i-1} a_{i,j}x_j - \sum_{j=i+1}^{n\times m} a_{i,j}XO_j + b_i\right)}{a_{i,i}}$$

(A1.37)

Where, x_i is the value corresponding to the ith position in the column vector $\vec{X}$. XO_i is the initial estimate, $a_{i,j}$ is the element corresponding to the ith row and j^{th} column in the matrix A and b_i, is the value corresponding to the ith position in the column vector $\vec{B}$. The above process was repeated until the iteration error was reduced to a value lesser than 0.01. The difference in accuracy was only 0.5% when the precision was varied between 0.0001 and 0.01; hence, to decrease the solution time, the tolerance of 0.01 was selected. Once the value of $\vec{X}$ was obtained, the values were substituted in the equation, and the approximation of induced drag was obtained as:

$$D_i = \frac{\rho}{2}\sum_{i=2}^{n-1}\sum_{j=2}^{m-1}\left(\psi_{i,j}\zeta_{i,j} - \phi_{i,j}\sigma_{i,j}\right)\eta^2$$

(A1.38)